Inaugural dissertation

for

obtaining the doctoral degree

of the

Combined Faculty of Mathematics, Engineering and Natural Sciences

of the

Ruprecht - Karls - University

Heidelberg

Presented by

M. Sc.Yuanyuan Wang

Born in: Hebei, P.R. China

Oral examination: 10th of February, 2023

Plasmatic von Willebrand factor regulates hematogenous metastasis of melanoma cells through its binding to heparan sulfate

Referees: Prof. Dr. rer.nat. Viktor Umansky

Prof. Dr. med. Stefan W. Schneider

Table of Contents

3 Results

Table of Figures

Abstract

Systemic spread of tumors is efficiently limited by the host system through the clearance of blood circulating cancer cells. However, cancer cells that evade host recognition are prone to form metastasis. In the present work, the contribution of plasmatic von Willebrand factor (vWF) to recognize blood floating melanoma cells was investigated. I found that blood circulating melanoma cells exposing heparan sulfate (HS) at their surface were strongly encapsulated by plasmatic vWF. Reduced length of the HS chains or complete lack of HS was associated with significantly reduced vWF recognition. Assisted by super resolution microscopy, I concluded that vWF formed a tight molecular complex with HS at the cancer cell surface. In microfluidic experiments, mimicking a tumor-activated vascular system, it was demonstrated that vWF-HS complexes prevented vascular adhesion. Single molecular force spectroscopy suggested that the vWF-HS complex promoted the repulsion of circulating cancer cells from the blood vessel wall. Experiments in vWF knockout mice further confirmed that the HS-vWF complex attenuates hematogenous metastasis, whereas melanoma cells lacking HS evade the antimetastatic recognition by vWF. In line with this, analysis of tissue samples obtained from melanoma patients indicated that metastatic melanoma cells produce less HS. Transcriptome data further suggest that attenuated expression of HS-related genes correlates with metastases and reduced patients' survival. In conclusion, I have shown that HS-mediated recognition of cancer cells by vWF can reduce their hematogenous spread. My data envisioned that therapeutic promotion of the vWF-HS interaction at the surface of cancer cells may attenuate metastasis.

Zusammenfassung

Die systemische Ausbreitung von Tumoren wird vom Wirtssystem durch die Beseitigung von im Blut zirkulierenden Krebszellen wirksam begrenzt. Krebszellen, die sich der Erkennung durch den Wirt entziehen, haben die Möglichkeit Metastasen zu bilden. In der hier vorliegenden Arbeit habe ich den Beitrag des plasmatischen von Willebrand Faktors (vWF) zur Erkennung von im Blut zirkulierender Melanomzellen untersucht. Ich fand heraus, dass Melanomzellen, die Heparansulfat (HS) an ihrer Oberfläche aufweisen, von plasmatischem vWF eingekapselt werden. Eine verringerte Länge der HS-Ketten oder das völlige Fehlen von HS ging mit einer deutlich verringerten vWF-Erkennung einher. Mit Hilfe hochauflösender Mikroskopietechniken kam ich zu dem Schluss, dass vWF einen engen molekularen Komplex mit HS an der Krebszelloberfläche bildet. In mikrofluidischen Experimenten, die ein tumoraktiviertes Gefäßsystem nachahmen, stellte ich zudem fest, dass vWF-HS-Komplexe die Gefäßadhäsion verhindern. Einzelmolekulare Kraftspektroskopie Messungen deuteten darauf hin, dass der vWF-HS-Komplex die Abstoßung zirkulierender Krebszellen von der Blutgefäßwand fördert. Experimente mit vWF-Knockout-Mäusen bestätigten außerdem, dass der HS-vWF-Komplex die hämatogene Metastasierung abschwächt, während Melanomzellen, denen HS fehlt, sich der antimetastatischen Erkennung durch vWF entziehen. Die Analyse von Gewebeproben von Melanompatienten ergab, dass metastasierende Melanomzellen weniger HS produzieren. Transkriptomdaten zeigten, dass eine verminderte Expression von HS-verwandten Genen mit der Bildung von Metastasen und einer geringeren Überlebensrate der Patienten korreliert. Zusammenfassend habe ich gezeigt, dass die HS-vermittelte Erkennung von Krebszellen durch vWF deren hämatogene Ausbreitung verringern kann. Meine Daten lassen vermuten, dass eine therapeutische Förderung der vWF-HS-Interaktion an der Oberfläche von Krebszellen die Metastasierung abschwächen kann.

Abbreviations

ADAMTS13 : A disintegrin-like and metalloproteinase with thrombospondin type 1 motif 13

AFM : Atomic force microscopy

CHPF : Chondroitin sulfate synthase 2

CHSY : Chondroitin sulfate synthase

CS : Chondroitin sulfate

CTCs : Circulating tumour cells

EC : Endothelial cell

ECIS : Electric cell-impedance sensing

ECM: Extracellular matrix

EMT : Epithelial mesenchymal transition

EVs : Extracellular vesicles

EXT1 : Exostosin 1

EXT2 : Exostosin 2

FBS : Fetal bovine serum

FGF : Fibroblast growth factor

GAGs : Glycosaminoglycans

GlcA : Glucuronic acid

GLCE : D-glucuronyl C5-epimerase

GlcNAc : N-acetylglucosamine

HA : Hyaluronic acid

Abbreviations

HAS : Hyaluronan Synthase

HP : Heparin

HPSE : Heparanase

HRP :horse reddish peroxidase

HS : Heparan sulfate

HS2ST1 : Heparan sulfate 2-O-sulfotransferase 1

HS6ST1 : Heparan-sulfate 6-Osulfotransferase 1

HUVECs : Human umbilical vein endothelial cells

HYAL : Hyaluronidase

IdoA : Iduronic acid

NDST4 : Bifunctional heparan sulfate Ndeacetylase/ N-sulfotransferase 4

NP : Nanoparticle

PAM : Protospacer adjacent motif

PD-1 : Programmed cell death protein 1

PD-L1 : Programmed death-ligand 1

PEG : Polyethylene glycol

PFA : Para-formaldehyde

RICM : Reflection interference contrast microscopy

SAW : Surface acoustic wave

SDC : Syndecan

SMFS : Single molecular force spectroscopy

Abbreviations

STED : Stimulated emission depletion

Sulf2 : Human Sulfatase 2

ULvWF : Ultra-large vWF

VCAM1 : Vascular cell adhesion protein 1

VEGF : Vascular endothelial growth factor

VLA4 : Very late antigen 4

vWF : von Willebrand factor

WGA : Wheat germ agglutinin

1 Introduction

1.1 The structure and function of glycocalyx

The glycocalyx is a nanometric mesh of carbohydrates covering every mammalian cell. The structure of the glycocalyx is highly divers comprising branched and un-branched carbohydrates[1], which is divided into five main type glycosaminoglycans (GAGs) (Figure 1): non sulphated GAGs, such as hyaluronan (HA), and sulfated GAGs, including Heparan sulphate/ heparin[2] (HS/HP), chondroitin sulphate[3]/ dermatan sulphate[4] (CS/ DS), and keratin sulphate[5] (KS). HS is considered to be the most abundant GAG, accounting for 50-90% of the total GAGs exposed e.g., by endothelial cells[1, 6-11]. The glycocalyx is involved in the crosstalk with the extracellular environment [12], including the interaction with a wide range of proteins, growth factors, cytokines, and adhesion molecules. Those interactions mediate many physiological functions, such as signalling processes, catalytic activities of enzymes and cell adhesion [13].

In the last years, it becomes evident that the glycocalyx is actively involved in signalling processes that drive malignancy and it has previously shown that increased levels of HS on melanoma cells attenuated lung metastasis in mice[14]. These results have recently been confirmed by others suggesting that an extended glycocalyx may prevent integrin activation and thus metastasis[15]. Although the explicit role of the GAG chain length on integrin activation is unknown, previous publications indicate that elevated HS levels prevent integrin activation, which would counteract cell adhesion [16].

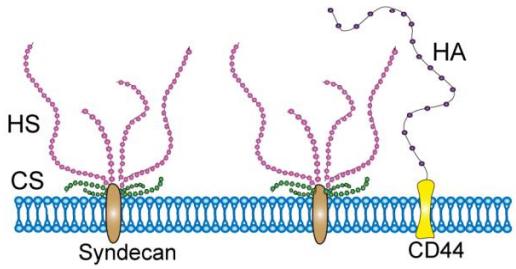

Figure 1. Schematic representation of the main components of the glycocalyx.

HS and CS are covalently attached to syndecans (SDCs). Hyaluronic acid (HA) is non-covalently linked to the plasma membrane via CD44. Adapted from **Wang, Y.** *et al.*, 2022[17].

1.2 The structure and function of heparan sulfate

HS is a glycosaminoglycan. The chain of HS is built by alternate additions of glucuronic acid (GlcA) and N-acetyl glucosamine (GlcNAc) forming a disaccharidic unit. At later stages of the HS biosynthesis, GlcA can be transferred into its epimer iduronic acid (IdoA). Every building block can be further modified by different sulfotransferases at different positions, producing a strongly negatively charged polymer. A total of 48 unique disaccharides possibilities have been reported[18, 19]. The biosynthesis and postsynthesis processing of HS is a complex process that involves the consecutive action of 11 different enzymes[18]. Figure 2 shows the biosynthesis of HS schematically. After synthesis of the linker region at the protein backbone, the HS chain is elongated by the action of the two glycosyltransferases exostosin 1 (EXT1) and EXT2 producing chains with a total length in the hundred-nanometer range[20]. Once exposed at the cellular surface, HS could be further processed through degradation or desulfation by the action of heparanase (HPSE) or sulfatases, respectively[14]. At each modification step only a fraction of the HS is processed. The result is a linear polysaccharide of considerable structural diversity.

In the course of HS biosynthesis, which takes place in the Golgi apparatus of mammalian cells, the HS chain is covalently attached to one of several types of core protein, to form heparan sulfate proteoglycans (HSPGs). HSPGs can be expressed at the cell membrane, released into the extracellular matrix (ECM)[21] or secreted in extracellular vesicles (EVs)[22, 23]. The two most abundant types of cell surface HS core protein are the trans-membrane SDCs and the GPI-anchored glypicans. The syndecan (SDC) family has four members (SDC1-4) and the number of HS chains they expose ranges from two to four. [24, 25]

HS forms, in concert with other glycocalyx components, a considerable gel-like layer that controls the communication of the cell with the extracellular environment. Over the last decade, HS have been extensively studied, and their interactions with growth factors, morphogens, chemokines, extracellular matrix (ECM) proteins and their bioactive fragments, receptors, lipoproteins and pathogens are well described[26, 27]. The group around Sylvie Richard-Blum generated a comprehensive overview of glycosaminoglycan interactome[28]. They compile the information of 580 HS binding proteins. Accordingly, HS can influence various physiological and pathophysiological process including e.g. hemostasis, extracellular

matrix organization, the immune system and several signal transduction processes such as VEGF recognition[29, 30].

Previous research showed that HS is binding to lysine/arginine residues aligned in the so-called “Cardin-Weintraub” sequences. The interaction is mediated by electrostatic forces[31]. However, binding affinities and specificities depend not only on electrostatic interaction forces but also on the conformation of the HS biding site and the structure of the HS. For instance, the binding of growth factors such as vascular endothelial growth factor (VEGF) or fibroblast growth factor (FGF) to heparin accept a variable HS structure, although the binding strength and biological activities is affected by the patter of sulfation[32]. Previous study suggested that HS binding is not a strictly linear function of charge[20]. HS chains with high negative charge densities were shown to cause counterion condensation[33]. The related screening of the negative charges abolished electrostatic interactions leading to a paradoxic effect, because highly charged HS chains attenuate their binding capacity. Therefore, cells with higher HS densities may be shield from the extracellular space and reduce the crosstalk of the cell with its environment.

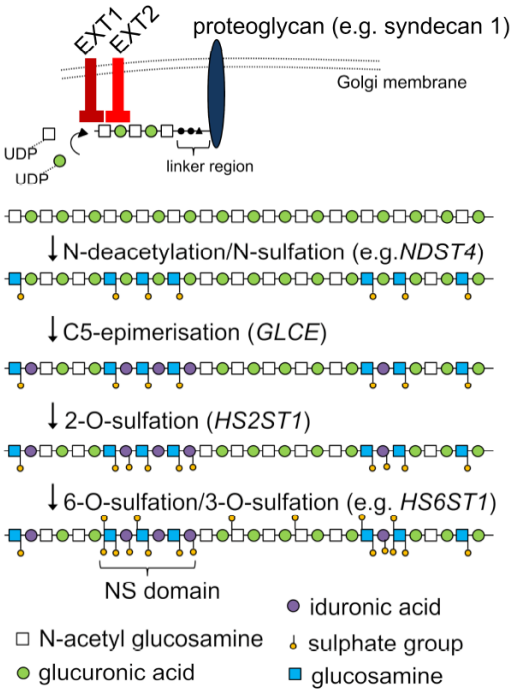

Figure 2. Key enzymes involved in HS synthesis and modification.

Schematic presentation of the HS chain elongation by EXT1 and EXT2 within the Golgi apparatus and the consecutive action of HS modifying enzymes. NDST4: Bifunctional

heparan sulfate Ndeacetylase/ N-sulfotransferase 4; GLCE: D-glucuronyl C5-epimerase; HS2ST1: Heparan sulfate 2-O-sulfotransferase 1; HS6ST1: Heparan-sulfate 6-Osulfotransferase 1. Modified after Li and Kusche-Gullberg[18].

1.3 Heparan sulfate proteoglycans in tumor metastasis

HS can bind cytokines and growth factors, which can control the behavior of tumor cells adhesion, migration, intravasation, survival during blood stream transit and extravasation[34]. Cancer cell behavior appears to be largely affected by the aberrant synthesis of HS due to a pathophysiological expression of enzymes involved in HS biosynthesis and post-synthesis modifications[35, 36]. We have recently shown that cancer cells produce an altered HS and that approximately 40% of all melanoma patients suffer from genetic alterations within the biosynthesis machinery of HS[20]. I also demonstrated that the overexpression of Human Sulfatase 2 (Sulf2) in the human breast cancer cell line MDA-MB-231 inhibited invasion and metastasis *in vitro* and *in vivo*[37].

As the core protein of HS, SDCs were also involved in the regulation of tumor metastasis. It had been demonstrated that loss of SDC1 in esophageal squamous cell carcinomas are closely associated with its malignant potential[38]. However, cell-surface HSPGs, especially SDC1, had also been reported to be strongly up-regulated in late-stage (malignant) breast cancer tissue[39]. Additionally, it was observed that SDC1 can promote tumor growth while others showed inhibition of metastasis underlining the complexity of HSPG and its co-receptor signalling capacity [34].

Moreover, the amount of HS can also be affected by HPSE, which can catalyzes the cleavage of HS into some smaller pieces. HPSE have been shown to play an important role in promoting the migration and metastasis of various cancer cells of different entities[40]. It has previously been reported that down regulated HPSE in melanoma cells, which resulted in elevated levels of HS at the cellular surface, attenuated hematogenous metastasis[14]. Although reduced HPSE activity diminished the availability of VEGF-A, the number of functional blood vessels and the rate of blood perfusion was increased[14]. The inflammatory profile was correlated with HS levels by increasing tumoral concentration of chemokine (C-

X-C motif) ligand 9 (CXCL9), CCL2 and vascular cell adhesion protein 1 (VCAM1). Tumor CXCL9 gradient was shown to be relevant for the recruitment of tumor infiltrating CD8+ T cells and the inhibition of tumor growth[41, 42]. Higher levels of CXCL9 can increase patients' response towards immune checkpoint therapy. In line with that, enhanced HPSE mRNA expression correlate significantly with increased metastases and decreased survival in patient with pancreatic and bladder cancer[43, 44].

1.4 The dissemination and adhesion of circulating tumor cells during metastasis

The metastasis of melanoma cells into distant organs such as the lung or brain is a common complication in late stage melanoma patients and is strongly associated with a reduced survival[45]. Metastasis begins with intravasation into the vascular system, subsequently, cancer cells are exposed to a number of harsh conditions in circulation, comprising fluid shear stress, hypoxia, the immune and coagulation system. Escape from this detrimental environment defines the ability of circulating tumor cells (CTCs) to extravasate and to from metastatic foci[46]. Depending on their origin and their genetic repertoire, cancer cells developed different evasion strategies e.g. interacting directly or indirectly with platelets, immune cells and coagulation proteins to aid in their survival[47] and to facilitate the adhesion to the blood vessel wall and the transmigration into the adjacent tissue[48]. Within a few minutes of their dissemination, CTCs can interact with platelets. Platelet derived TGF-β can promote epithelial mesenchymal transition (EMT), which is crucial for the formation of the initial metastatic niche[49]. Platelets and coagulation proteins can protect CTCs from fluid shear stress through the creation a rich cell surrounding microthrombi[50]. CTCs evade immune detection through the expression of programmed death-ligand 1 (PD-L1) receptor and by interacting with T-Cell programmed cell death protein 1 (PD-1)[51, 52]. The expression of CD47 enables CTCs to escape macrophage-mediated phagocytosis[53]. After escaping from elimination in vascular system, CTCs with the capacity to metastasize transmigrate across the endothelial barrier [54]. Under homeostatic condition, the surface of the endothelium is repulsive preventing the adhesion and passage of e.g. CTCs and immune cells. However, the activated endothelium, in response to tumor-secreted angiogenic factors or inflammatory

signals, upregulates adhesion molecules to support the adhesion of CTCs and increases vascular permeability enabling the transmigration of CTCs.

Over the past decades, several mechanisms underlying tumor-endothelial interaction have been reported. Previous study showed circulating melanoma cells expressed very late antigen 4 (VLA4) partly drive the interaction with the endothelial vascular cell adhesion molecule (VCAM) 1, which is highly expressed on the surface of an activated endothelium [55, 56]. Interaction of cell adhesion molecule Thy-1 (CD90) with the integrin αvβ3 (CD51/CD61) is also an important mechanism mediating vascular adhesion of melanoma cells [57]. Additionally, E- and P-selectins on the luminal surface of endothellial cells promote metastasis formation by interacting with sialyl-Lewis X and A (sLeX/sLeA) exposed by CTCs. This interaction further precedes extravasation, and promotes metastasis formation[58]. Our previous work also shown ultra-large von Willebrand factor (ULvWF) fibers functions as an adhesion molecule for CTCs through platelet-mediated aggregates and microvascular occlusion[59], and further facilitate cancer cell extravasation and metastasis.

1.5 The structure and role of von Willebrand factor

VWF is a large multimeric glycoprotein found in the peripheral blood stream, it performs important haemostatic functions. First, vWF is involved in secondary hemostasis as it binds and serves as a carrier for coagulation factor VIII. Second, it traps blood flowing platelets, at sites of vascular injury, therefore initiating primary hemostasis[60]. Under physiological conditions, vWF biosynthesis is restricted to endothelial cells (ECs) and megakaryocytes. Quiscent ECs secete vWF constitutively into the subendothelial matrix, while activated EC release vWFinto the blood flow [61-63]. After secretion, vWF multimers remained anchored to the EC surface and, when exposure to shear stress, they can form ULvWF fiber networks. Non-anchored vWF or ADAMTS13 (a disintegrin and metalloproteinase with a thrombospondin type 1 motif, member 13) shedded ULvWF becomes part of the plasmatic vWF pool. In circulation, plasma vWF reversibly transforms from a globular to a stretched conformation and exposes binding sites, for example the heparin within the A1 domain as well as the cleavage site within the A2 domain for ADAMTS13 [64-68]. Normally, the hemostatic active vWF multimers are rapidly cleaved by ADAMTS13 into smaller less active vWF

fragments [69]. To keep homeostasis, plasma vWF is steadily cleared by Kupffer cells within the liver[70].

1.6 The role of von Willebrand factor in tumor metastasis

In addition to the well-known functions of vWF in maintaining normal homeostasis, more recently novel biological functions of VWF in tumor progression have been described. Studies have shown that vWF can promote pro-inflammatory signalling, regulate angiogenesis and vascular permeability[71]. VWF has been identified as having both pro- and anti-angiogenic roles. For example, knockdown of vWF expression in ECs resulted in increased proliferation and migration in response to VEGF[72]. In line with this, vWF-/- mice displayed increased vascularization. While, paradoxically, reduced arteriogenesis and angiogenesis were observed also in vWF-/- mice. Moreover, vWF also had long been hypothesized to contribute to cancer metastasis[73]. However, the potential role of vWF in malignancy has raised some controversy.

Our previous work demonstrated that in malignant melanoma of both human and mice, ULvWF fibers were shown to promote cancer-platelet heteroaggregates and microvascular occlusion[59]. These data suggested that ULvWF stings can recruit platelets, thereby contributing to the increased risk of thrombosis observed in cancer patients. The ULvWF strings may function as an adhesive anchor for CTCs and thus facilitate cancer cell extravasation and metastasis. VEGF-A released from breast cancer cells was shown to induce secretion of vWF multimers from the endothelium and further mediating the vascular adhesion of breast cancer cells [74]. Further, *in vivo* multiphoton laser scanning microscopy showed vWF clot formation as a prerequisite for the extravasation of breast cancer cells into the brain[75]. Intraluminal vWF fibers were discovered in a murine model of melanoma not only in primary tumors, but also in tumor-free distal organs, which tumors frequently metastasize[76]. Experiments in ADAMTS13-deficient mice, characterized by prolonged lifetime of ULvWF fibers, showed more lung metastasis [76], also suggesting a pro-metastatic role of ULvWF.

In line with that plasma vWF, as an acute phase inflammatory marker, clinical observations have demonstrated a positive correlation between cancer progression and elevated plasma vWF antigen levels [77-81,73]. To directly show the role of vWF in tumor progression, previous studies were performed in VWF genes deficient mice. By using vWF knockout mice which present the total depletion of vWF (ULvWF and plasmatic vWF), it was demonstrated that vWF-deficiency promoted pulmonary metastasis [76, 82]. And what is more, Terraube *et al.* also showed, by restoring plasma vWF that the phenotype could be corrected to the similar amount of metastasis as found in wild-type mice [82]. Those *in vivo* experiment clearly suggested an anti-metastatic role of plasma vWF and were in contrast to the clinical observations. The acting molecular mechanisms mediating the anti-metastatic behaviour of plasmatic vWF are largely unknown although it was speculated that VWF may induce apoptosis of cancer cells through binding to αvβ3, which subsequently leads to the phosphorylation of p53, activation of caspase 3[83].

In summary, different findings underscore the complexity of vWF in cancer and suggest that there are multiple ways how vWF may affect the progression of tumors and metastasis. What's more, previous data suggest that ULvWF and plasma vWF might play different roles in tumor progression.

1.7 Aims of study

HS is a strongly negatively charged carbohydrate, which coats most mammalian cell. As such, HS is fundamental for the communication of the cell with the extracellular environment. Those communications have also been shown to play important roles in tumor cell migration and metastasis. Over the last decade, new insights have emerged regarding the mechanisms and the biological significance of those interactions[84, 85]. HSPGs are co-receptor of many different signaling processes that may affect tumor progression and metastasis, which are however not yet explored in detail[86]. Therefore, in my present work, I aimed to apply various methods ranging from *in silico*, *in vitro* to *in vivo* assays to study the pathophysiological relevance of cellular HS in the context of metastasis.

The presence of CTCs in blood has been largely associated with cancer progression[87-89]. Moreover, CTCs are well accepted as the start point for metastasis and their presence identifies patients with a higher risk of developing metastasis[90, 91]. To form successful metastasis, firstly, CTCs need to resist the physical and biological challenges in the bloodstream. The effective number of CTCs is low, since less than 0.01% of the tumor cells exposed to blood can avoid being killed by the immune system through interacting with blood components [92] In the past, the ability of CTCs to interact with platelets, neutrophils, NK cells, macrophages and other immune cells has been studied and linked to pathophysiological processes[92, 93]. However, the interplay of CTCs with plasma proteins and the related molecular consequences remained largely unexplored[47].

VWF is the largest multimeric plasma glycoprotein in mammalians and the only known plasma molecule whose binding capacity is strongly enhanced under blood flow conditions. Interestingly, plasma vWF levels are increased in cancer patients and have been proposed as promising biomarker predicting disease severity and patients' outcome [94, 95,75, 96-100]. Despite the increasing amounts of reports suggesting plasmatic vWF as a biomarker, no previous study has tackled its pathophysiological role on the CTC level. Now, my data provide first evidence that plasmatic vWF in combination with cellular HS exhibit a disease protective function limiting hematogenous dissemination of CTCs.

Different independent studies have showed vWF can directly bind to a variety of tumor cell lines [82, 101-103], and the interaction with αvβ3, αvβ5 integrins may play an important role. However, recent research emphasized that integrin accessibility and activity is strongly regulated by the glycocalyx of the tumor cell [16, 104, 105]. Interestingly, previous research suggests also that the cellular glycocalyx is by itself a potential vWF binding partner [106] However, so far, data on the triangular crosstalk between HS, integrins and the plasmatic vWF are still lacking. Here, distinct vWF mutants were used to study the impact of tumor cell exposed HS and integrin on vWF accumulation, and its role during haematogenous metastasis.

Melanoma is one of the most aggressive forms of skin cancer. High capacity of metastases is malignant melanoma´s main characteristics. Despite screening and early detection programs, the overall mortality rate from melanoma has remained stable or continues to rise[107-109].

Although recent data demonstrate the contribution of HS to melanoma malignancy[86], the mechanism that might promote melanoma metastasis has not yet been explored. Therefore, melanoma patients' biopsies and transcriptome data were also used, to investigate the pathophysiological relevance of cellular HS in the context of melanoma patient progression.

2 Material and Methods

2.1 Materials

2.1.1 Chemicals

Chemicals Name	Company	Catalog NO.
Recombinant Mouse P-Selectin/CD62P Fc Chimera Protein, CF	R&D Systems	737PS050
Recombinant VLA4	R&D systems	5668-A4
Recombinant VCAM1	R&D systems	862-VC
His-tagged VLA4	R&D systems	5668-A4-050
Bio5192	TOCRIS	327613-57-0
Fibronection	Sigma-Aldrich	F0556
heparinase I and II	Sigma-Aldrich	H3917
hyaluronidase	Sigma-Aldrich	H3884
chrondroitinase ABC	AMS Biotechnology	100332-1A
Cilengitide	Merck	188968-51-6
Tinzaparin	Innohep	NDC 50222-342-08
unfractionated heparin	Merck	375095
ethoxy silane polyethylene glycol acid	Nanocs	PG2-CASL-5k
TNFα	R&D systems	10291-TA-020
^{35}S-sulfate	Perkin Elmer	NEX041H001MC
chondroitinase ABC	Seikagaku	100332-1A
Superose 6 HR10/30 column	Amersham Biosciences	GE17-5172-01
Fluoromount G	Southern Biotech	0100-01
Lipofectamine 2000	Thermo Fisher Scientific	11668027
TMB substrate reagent set	R&D System	BD 555214
DPBS	Thermo Fisher Scientific	14040141

2.1.2 Kits

Product Description	Company	Catalog NO.
RNeasy Plus Mini Kit	Qiagen	74106
Reverse Transcription System	Promega	A3500
GoTaq qPCR Master Mix	Promega	A6001/2
Alt-R Genome Editing Detection Kit	Integrated DNA Technologies	1075931

2.1.3 Antibodies

Primary antibodies	Company	Catalog NO.
Rabbit anti-Human vWF	Dako Denmark A/S	A0082
Wheat Germ Agglutinin, Alexa Fluor™ 647 Conjugate	Thermo Fisher Scientific	W32466
Wheat Germ Agglutinin, Alexa Fluor™ 488 Conjugate	Thermo Fisher Scientific	W11261
Ab Heparan Sulfate, purified (clone F58-10E4)	AMS Biotechnology	370255-1
Anti-Integrin beta3 antibody	Novus Biologicals	NBP2-67416
Anti-S100 Protein rabbit polyclonal, serum	Progen	16100
Anti-VCAM1 antibody	Abcam	Ab134047
Secondary antibodies		
Alexa Fluor® 647 goat anti-mouse IgM	Thermo Fischer Scientific	AB_2535807
Alexa Fluor® 647 Goat anti-Rabbit IgG	Thermo Fischer Scientific	A32733
Rabbit anti-Human vWF/HRP	Dako Denmark A/S	P0226

2.1.4 Primers

Integrin 2b	Forward	5′- CAT GGT TCA ACG TGT CCT CC -3′
	Reverse	5′- TCA TCT TCT TCC AGG GGT GG-3
Integrin αv	Forward	5′- ATC TGT GAG GTC GAA ACA GGA -3′
	Reverse	5′- TGG AGC ATA CTC AAC AGT CTT TG -3′
Integrin β3	Forward	5′- ACC AGT AAC CTG CGG ATT GG -3
	Reverse	5′- TCC GTG ACA CAC TCT GCT TC -3′
Integrin β5	Forward	5′- GGA AGT TCG GAA ACA GAG GGT -3′
	Reverse	5′- CTT TCG CCA GCC AAT CTT CTC -3′
Integrin α4	Forward	5′- AGC CCT AAT GGA GAA CCT TGT -3′
	Reverse	5′- CCA GTG GGG AGC TTA TTT TCA T -3′;
Integrin β1	Forward	5′- CAA GAG AGC TGA AGA CTA TCC CA -3′
	Reverse	5′- TGA AGT CCG AAG TAA TCC TCC T -3′
Integrin (murine) α4	Forward	5′- GAT GCT GTT GTT GTA CTT CGG G -3′
	Reverse	5′- ACC ACT GAG GCA TTA GAG AGC -3′
Integrin (murine) β1	Forward	5′- ATG CCA AAT CTT GCG GAG AAT -3′
	Reverse	5′- TTT GCT GCG ATT GGT GAC ATT -3′
Integrin (murine) αv	Forward	5′- AAA GAC CGT TGA GTA TGC TCC A -3′ a
	Reverse	5′- ATG CTG AAT CCT CCT TGA CAA AA -3′;
Integrin (murine) β3	Forward	5′- GGC GTT GTT GTT GGA GAG TC -3′
	Reverse	5′- CTT CAG GTT ACA TCG GGG TGA -3′
Integrin (murine) β5	Forward	5′- CAG GTG GAG GAC TAC CCT GTA -3′
	Reverse	5′- CGA AAC CTA AGC GGA AGT TAC T -3′
Thy-1	Forward	5′- ATC GCT CTC CTG CTA ACA GTC -3′
	Reverse	5′- CTC GTA CTG GAT GGG TGA ACT -3′
EXT1	Forward	5′-GAG ACA ATG ATG GGA CAG ACT TC-3
	Reverse	5′-CTC TGT CGC TGG GCA AAG-3′
EXT2	Forward	5′-CTG GGA CCA TGA GAT GAA TA-3′
	Reverse	5′-GAT ATC CCC AGG CAT TTT GTA-3′;
HPSE	Forward	5′-ATG CTC AGT TGC TCC TGG AC-3′
	Reverse	5′-CTC CTA ACT GCG ACC CAT TG-3′

SDC1	Forward	5′-CTC AGG TGC AGG TGC TTT G-3′
	Reverse	5′-CTG CGT GTC CTT CCA AGT G-3′
SDC2	Forward	5′-GAT GAC GAT GAC TAC GCT TCT G-3′
	Reverse	5′-TGG AAG TGG TCG AGA TGT TG-3′
SDC3	Forward	5′-CTC CTT TCC CGA TGA TGA AC-3′
	Reverse	5′-CGA CTC CTG CTC GAA GTA GC-3′
SDC4	Forward	5′-GGC AGG AAT CTG ATG ACT TTG-3′
	Reverse	5′-TCT AGA GGC ACC AAG GGA TG-3′
HAS1	Forward	5′-TGC TCA TCC TGG GCC TCA T-3′
	Reverse	5′-AAT CTC CGA GCG CCT TGA A-3′
HAS2	Forward	5′-AGT TGC CCT TTG CAT CGC T-3′
	Reverse	5′-AGA CTG ACA GGC CCT TTC T-3′
HAS3	Forward	5′-ACC AGT TCA TCC ACA CGG-3′
	Reverse	5′-ACC TGG ATG TAG TCC ACC GA-3′
HYAL1	Forward	5′-ATA GCT CCC AGC TGG GCA-3′
	Reverse	5′-AGA TTG GGG TCA CCA GCA-3′
HYAL2	Forward	5′-TTG ATG TGC AGG CCT CAC CTA-3′
	Reverse	5′-CTC CTT AAT GTC ACG CAC GAT-3′
CHSY1	Forward	5′- GCCCAGAAATACCTGCAGAC-3′
	Reverse	5′- GCACTACTGGAATTGGTACAGATG-3′
CHPF	Forward	5′- GGTGCACTATAGCCATCTGGA-3′
	Reverse	5′- GGCACTTCGGAAATGAGG-3′
CHSY3	Forward	5′- GACTCAGTGTGTCTGGTCTTACG-3′
	Reverse	5′- TTGCTATTGTGAAGGTCTTGGA-3′

Expression levels were normalized to the endogenous β-actin gene (5′-CAT GTA CGT TGC TAT CCA GGC-3′ and 5′-CTC CTT AAT GTC ACG CAC GAT-3′).[17]

2.2 Methods

2.2.1 Cell lines and cell culture

The human melanoma cell lines MV3, and IGR37 were cultured in RPMI 1640 medium (Gibco, Life Technologies) with 10% FBS, 1% L-Glutamine and 1% penicillin/streptomycin. Mouse melanoma cell lines B16 were cultured in DMEM (Gibco, Life Technologies) with 10% FBS, 1% NEAA (Sigma-Aldrich), 1% L-Glutamine and 1% penicillin/streptomycin. The breast cancer cell line MDA-MB-231 and the circulating breast cancer cell line CTC-ITB-01 were kindly provided by Prof.Dr. Sabine Riethdorf and Leonie Ott (University Medical Center Hamburg-Eppendorf, Hamburg, Germany).

Human umbilical vein endothelial cells (HUVECs) were isolated from donor umbilical cord according to the ethical regulation (Ethics committee of the University Medical Center Hamburg-Eppendorf, Germany) and were cultivated in a 0.5% Gelatin (Sigma-Aldrich) coated surface in 100 mL culture medium containing 63mL M199 (Life Technologies), 30mL EGM-2 (LONZA) and 7mL fetal bovine serum (FBS), which was furthersupplemented with: 200 ng/mL hydrocortisone, 0.5 ng/mL VEGF, 10 ng/mL human FGF-2, 5 ng/mL human epidermal growth factor (EGF), 20 ng/mL human IGF-1, and 1 µg/mL ascorbic acid. The HUVECs isolation was done using our lab established protocol[110]. Only passages lower than 6 were used for all experiments.

All cell lines were cultured in an incubator at 37°C in a humidified 5% CO_2 atmosphere. The cells were passaged at a confluency of about 90% as previously reported[110].

2.2.2 Mouse experiments

VWF deficient mice were purchased from Jackson Laboratory. Wild type C57BL/6J mice and vWF deficient mice were kept under specific pathogen free conditions in the animal facility of the University Medical Center Hamburg-Eppendorf (UKE), Hamburg. 1×10^6 B16F10 $^{Ext1+/+}$ or B16F10 $^{Ext1-/-}$ transgenic melanoma cells in 100 µl PBS were injected into the tail vein of 8-12 weeks old mice. After 15 days of injection, mice were sacrificed and the metastatic foci

on the lung were counted. After taking photographs, lungs were embedded for cryosectioning (Tissue-Tek O.C.T. Compound).

All animal experiments were approved by the government animal care authorities and were done in accordance with the guidelines of the German law for the use and care of laboratory animals.

2.2.3 Melanoma patients' tissue

The samples of primary and metastatic melanoma tissues were obtained from malignant melanoma patients with the stage of UICC III and IV. The use of patient tissue samples was approved by the ethics committee of the University Medical Center Hamburg-Eppendorf.

2.2.4 Melanoma patients' data

The patients' overall survival data and mRNA expressions in melanoma patients were obtained from the cancer genome atlas (TCGA) project [111]. In total, 441 cutaneous melanoma patients with an average age of 58 ± 16 years were studied. In the cutaneous melanoma group, 81 samples were collected from primary melanoma and 367 samples were obtained from metastases. Further information is available on the cBioportal repository [112, 113] and the related original research [111]. To correlate patients' overall survival with the level of gene expression, Kaplan-Meier plots were used.

2.2.5 Flow cytometry

Cells were cultured and harvested. Prior to staining, cells were blocked with 10% goat serum for 30min, on ice. Then, direct staining of cell was performed by AlexaFluor 647-conjugated or AlexaFluor 488-conjugated WGA (Thermo Fisher Scientific 1:1000). Indirect staining was first using HS antibodies (10E4 epitope, AMS Biotechnology, 1:1000). Then, after washing with PBS, cells were further incubated with Alexa Fluor 647 goat anti-mouse IgM secondary antibody (Thermo Fischer Scientific, 1:1000). For all staining, cells were incubated with

antibodies for 30 min on ice. Finally, fluorescence intensity of cells was measured with flow cytometry (BD FACSCanto II, Biosciences). Data were analyzed by Flowing Software (version 2.5.1).

Flow cytometry was also used for static P-selectin binding experiments. Prior to incubation, recombinant chimeric murine P-selectin-IgG-Fc constructs (10 µg/mL, R&D Systems) were pre-complexed with biotin-linked anti-human IgG (Sigma-Aldrich) and allophycocyanin-(APC-) conjugated streptavidin (BD Bioscience). Subsequently, melanoma cells were incubated with the pre-complexed selectins for 20 min at 4°C. For isotype control, IgG-Fc fragments (R&D Systems) were used.

2.2.6 Immunofluorescence staining

Cells (seeded on coverslip previously) or tissue cryosections (10 µm) were first fixed with fixation reagent (4% para-formaldehyde, PFA) for 10 min. Prior to the staining, cells were blocked with 10% goat serum for 30min, at room temperature. Then, direct staining was done by primary antibodies conjugated with Alexa Fluor647 and/or AlexaFluor 488-conjugated WGA (Thermo Fisher Scientific 1:1000). For indirect staining cell were first incubated with HS antibodies (10E4 epitope, AMS Biotechnology, 1:1000), integrin beta3 (Novus Biologicals 1:200) or anti-S100 Protein rabbit polyclonal, (Progen 1:100). Then, after washing with PBS, cells were further incubated with secondary antibodies: Alexa 647-conjugated goat anti-mouse (IgM; Thermo Fisher Scientific, 1:5000) or Alexa 647-conjugated goat anti-rabbit (Thermo Fisher Scientific, 1:2000). Nuclei were stained with DAPI. Finally, the fluorescence intensity of samples was imaged with fluorescence microscopy (Observer z.1, Zeiss). Images were analyzed with Image J (version 1.52)[114].

2.2.7 The binding of vWF analyzed by Immunofluorescence

Cells were cultured and collected. 500,000 cells were counted and re-suspended with Dulbecco's Balanced Salt Solution (DPBS) (Thermo Fisher Scientific 14040141) containing calcium and magnesium. To measure the vWF binding capacity, cells were mixed with

different recombinant mutant or wild type vWF (40 µg/mL) in suspension. Where indicated cilengitide (10 µM) or Tinzaparin (Innohep, 100 U/mL) was added to the system. All incubations were performed at 37° C for 30 min.

Prior to staining, cells were fixed with fixation reagent (4% PFA) for 10 min and blocked with 1% BSA for 30min, at room temperature. Then, indirect staining procedure based on the vWF directed primary antibody (rabbit anti-human vWF, Dako Denmark A/S, 1:250). Then, after washing with PBS, cells were further incubated with the secondary antibody: Alexa 647-conjugated goat anti-rabbit (Thermo Fisher Scientific, 1:2000). For all staining, cells were incubated with antibodies for 30 min, at room temperature.

After staining, cells were re-suspended with the mounting medium, Fluoromount G (Southern Biotech). The cell suspension was dropped on object slides and mounted with coverslips. Fluorescence microscopy was performed using a Zeiss Observer z.1 microscope. Images were analyzed with Image J.

2.2.8 The binding of vWF analyzed by on-cell enzyme-linked immunosorbent assay (ELISA)

500,000 cells were collected and re-suspended with DPBS and incubated with different mutated vWF or wild type vWF (40 µg/mL) in suspension as previously described in 2.2.7. Prior to staining, cells were fixed with fixation reagent (4% PFA) for 10 min. and blocked with 1% BSA for 30min, at room temperature. Then, cells were incubated with horse reddish peroxidase (HRP)-conjugated rabbit anti-human vWF polyclonal antibody (Dako Denmark A/S, 1:2000) for 30 min, at room temperature. After washing three times with PBS, the cell pellet was re-suspended with 100 µl PBS and added to transparent 96-well plates. For detection, 100 µl TMB substrate solution (R&D System) was further added into the wells and incubated for about 10min in the dark. Finally, 50 µl of stop solution (1M H_2SO_4) was added into each well to stop the enzyme reaction. All the steps were performed at room temperature. Optical densities were measured in each well at the wavelength of 450nm using a microplate reader (BioteK PowerWave XS2 photometer).

2.2.9 Glycocalyx enzyme treatment

Cells were detached and collected. 1,000,000 cells were re-suspended in PBS with 0.1% bovine serum albumin (BSA). Cells were treated with different glycocalyx enzymes: heparinase I and II (Sigma-Aldrich, 500 mU/mL) to remove HS, hyaluronidase (Sigma-Aldrich, 150 mg/mL) to remove HA or chrondroitinase ABC (AMS Biotechnology, 500 mU/mL) to remove CS. For control, cells were incubated only in 0.1% BSA buffer. All the enzymatic reactions were performed at 37 °C for 3h.

2.2.10 Nanoparticle (NP) titration assay

To measure the amount and length of cell surface GAGs, NP titration was conducted as previously reported[20]. First, cells were treated with different GAGs degrading enzymes as described in 2.2.9. After digestion, 400 000 cells were counted and incubated with fluorescent chitosan NPs at different concentrations (1.12×10^{11}, 2.24×10^{11}, 4.48×10^{11}, 8.96×10^{11}, 1.78×10^{12} particles per mL) for 30 min at 37 °C. The binding of NP was detected by flow cytometry as described in 2.2.5. The dose-binding of NP to cell surface GAG was analyzed. Assist with stimulated emission depletion (STED) images the length of the HS chain was calculated.

2.2.11 Stimulated emission depletion (STED) microscopy

Immunofluorescence stained HS were imaged with STED microscopy which were conducted under similar conditions as previous studies[20]. The STED microscopy was carried out in sequential line scanning mode using an Abberior STED expert line microscope. A pulsed laser was used for excitation at wavelength of 640 nm. For detection, a near-infrared pulsed laser (775 nm) was used. Finally, images were recorded with a dwell time of 3 µs and the voxel size was set to 20×20×150 nm. Images were acquired in time-gating mode with a gating width of 8 ns and a delay of 781 ps.

2.2.12 Melanoma MV3 cells spiked with whole human blood

Human melanoma MV3 cells were collected and stained with the green fluorescent dye : CellTracker™ Green CMFDA (Thermo Fisher Scientific, 1:1000). Whole human blood was collected using hirudin as an anticoagulant. The labeled MV3 cells were then incubated with whole blood at 37° C for 30 min. The buffy coat containing melanoma cells and leukocytes was isolated by density gradient centrifugation using ficoll as previously reported[115]. Then, the cells from the buffy coat were stained with the primary antibody: rabbit anti-human vWF (Dako Denmark A/S, 1:250). Then, after washing with PBS, cells were further incubated with the secondary antibody: AlexaFluor 647-conjugated goat anti-rabbit (Thermo Fisher Scientific, 1:2000). Nuclei were stained with DAPI. For all staining, cells were incubated with antibodies for 30 min, at room temperature. After staining, cells were re-suspended with the mounting medium: Fluoromount G (Southern Biotech), cell suspension was dropped on object slides and mounted with coverslips. Fluorescence microscopy was performed using a Zeiss Observer z.1 microscope. Images were analyzed with Image J.

2.2.13 RNA extraction and qPCR

1,000,000 cells were detached and collected. Prior to RNA extraction using RNeasy Plus Mini Kit (Qiagen) as suggested by the manufacturer. The concentration of RNA was measured with a microplate reader (BioteK PowerWave XS2 photometer). The purity was evaluated by the ratio of absorbance at 260nm and 280nm. Then, cDNA was synthesized by using Reverse Transcription System (Promega) with procedures of 25°C 10 min, 50°C 15 min and 85°C 5 min. Subsequently, the GoTaq® qPCR Master Mix (Promega) system was used for qPCR reaction and reactions were running with a real-time PCR system (Light cycler 96 system, Roche). The primers used for qPCR are provided in Table 2.

2.2.14 Genome engineering of melanoma cells

For knockdown EXT1 expression, shRNA Plasmid Kit was purchased from origene, 4 unique human EXT1 shRNA and a scrambled shRNA were cloned into the pGFP-C-shLenti Vector

lentiviral GFP vector. For the production of lentiviral particles, the 3rd generation lentiviral packaging plasmid was used and experiment was performed as previously reported[116]. Finally, stably transduced cells were selected with puromycin (2 µg/mL).

For knockout EXT1 expression, CRISPR/Cas9 was used. First, sgRNAs were designed using the online CRISPR Design tool (http://crispor.tefor.net/). The target specific sequences of *Ext1* are 5'-CACCGAACATTCTAGCGGCCATCGA-3' and 5'-AAACTCGATGGCCGCTAGAATGTTC-3'. Then the synthesized sgRNAs were cloned into the pSpCas9(BB)-2A-Puro vector (Addgene #48139). The gRNA cloning vector constructs were transfected into the B16F10 murine melanoma cells using Lipofectamine 2000 (Thermo Fisher Scientific) as previously reported[117]. Transfected cells were cultured with puromycin (2 µg/mL) for 24h to select for stable *Ext1* knockout cell. The puromycin-resistant cells were further diluted serially in 96 well plate, and single cell clone was picked and cultured. Prior to gene sequencing, the gene editing was detected by the Alt-R Genome Editing Detection Kit (Integrated DNA Technologies). Primers using for gene sequencing were bracketing the targeted gene region (5'-GGAACCGTAGTGCTCTGCAC-3' and 5'-GAACATGTGTCTCTCTGAGTCG-3').

To rescue HS expression in *Ext1* knockout cells, full-length cDNA of the *Ext1* gene was cloned into the pLenti CMV/TO Puro vector (addgene #17482). The production of Lentivirus particles and transfection of B16F10 cells were performed as previously described[116]. The evaluation of HS expression in genetic engineered cells was performed by flow cytometry.

2.2.15 Endothelial cell adhesion under flow condition

Microfluidic experiment was used to study endothelium adhesion. First, HUVECs were isolated and cultured as described in 2.2.1. Then, fibronectin (Sigma-Aldrich, 50 ug/mL) was perfused at 2 dyn/cm^2 to coat BIOFlUX 200 48-WELL plate (Fluxion, 0-20 dyn/cm^2). After incubation for 1 h at room temperature, the plate was washed with ddH_2O and prewarmed Leibovitz's L-15 Medium (gibco 31415029), respectively. HUVECs were seeded on fibronectin coated microfluidic channels and cultured at 37° C and 0% CO_2 until confluent cell monolayer formation.

To induce the expression of VCAM1, HUVECs were stimulated with 10 ng/mL TNFα (R&D systems) at 37° C for 4h. Melanoma cells suspended ($1x10^6$ cells/mL) in prewarmed Leibovitz's L-15 Medium were perfused over the HUVEC-coatedmicrofluidic channel with or without the presence of vWF (20 µg/mL). The flow experiments were performed at a shear rate of 2 dyn/cm^2 using the BIOFLUX200 system (Fluxion). To study the adhesion molecules, VCAM1 neutralizing antibody (Abcam, 100 µg/mL), Bio5192 (TOCRIS, 100 µM) or Cilengitide (Merck, 10 µM) was also added to the system individually. Schematic drawing was shown in Figure 3. Adherent cancer cells were recorded by fluorescence microscopy (Observer z.1, Zeiss) and analyzed with Image J.

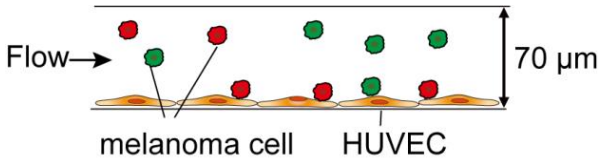

Figure 3. Schematic painting of the microfluidic setup.

HUVECs were coated on the bottom of fibronectin coated BIOFLUX plate. After stimulating with TNFα for 4 hs, melanoma cells were perfused under the shear flow of 2 dyn/cm^2. The adhesion of melanoma cells was recorded. Adapted from **Wang, Y.** *et al.*, 2022[17].

2.2.16 P-selectin adhesion under flow condition

The dynamic adhesion of melanoma cells to murine P-selectin was also studied with microfluidic assay as previously described[118, 119]. First, recombinant murine P-selectin/IgG1-Fc chimeras (rmP-Sel, R&D Systems, 20 µg/mL) were coated to ibidiTreat µ-slide $IV^{0.4}$ flow chambers (ibidi GmbH) at the shear rate of 0.25 dynes/cm^2 using the BIOFLUX200 system (Fluxion). After incubation for 30min at room temperature, melanoma cell suspension ($1x10^5$ cells/mL) were perfused to the chamber at a shear stress of 0.25 dynes/cm^2. IgG1-Fc fragments were used as negative control (R&D Systems). Adherent cancer cells were acquired and analyzed with CapImage software (version 8.6, Dr. Heinrich Zeintl, Heidelberg).

2.2.17 Electric cell-impedance sensing (ECIS)

To measure the height of HS proteoglycans, ECIS was performed as previously reported[20]. Firstly, gold electrodes slides (8W10E+ PET, Applied Biophysics, New York, USA) were coated with fibronectin (10 µg/mL) for two hours at room temperature. After the incubation, fibronectin was removed and slides were washed with PBS. Then, stabilize electrodes in the ECIS instrument (ECIS Z theta, Applied Biophysics, New York, USA). 200,000 B16F10 cells per well at the final volume of 400 µl were seeded. The slides were connected to the ECIS instrument and the impedance spectra ranging from 500 to 64000 Hz were recorded every 48s for 24h. ECIS experiments were measured in an incubator with humidified atmosphere and 5% CO_2 at 37°C. Cell impedances were analyzed and the distance of the cells from their substrate was calculated assuming a rectangular cell shape as previously shown by Giaever and Keese[120].

2.2.18 Reflection interference contrast microscopy (RICM)

The distance of the adhering cells to the substratum was measured with RICM. Prior to cells seeding, fibronectin (100 µg/mL) was coated to an eight-chamber microscopy slide (ibidi GmbH). Then, 50,000 melanoma cells per well were seeded. Immediately after seeding, the eight-chamber slide was placed on the RICM stage (z1 Observer, Zeiss, Oberkochen, Germany). Images were taking continuous. During the RICM experiments, cells were kept with humidified atmosphere and 5% CO2 at 37°C. Distance of the ventral side of the cell to the substratum was measured at a wavelength (λ) of 480 nm. Mean light intensity per cell (I_{cell}), minimum light intensity per cell (I_{min}), minimum light intensity per field of view ($I_{min,fov}$) and maximum light intensity per field of view ($I_{max,fov}$) was determined by imageJ. The average distance (d) of the adhering cells from the substratum was calculated by $d = (I_{cell} - I_{min}) \lambda / 2(I_{max,fov} - I_{min,fov})$.

2.2.19 Single molecule force spectroscopy (SMFS)

To mimic the approach of melanoma cells to endothelium, SMFS measurement was performed with an atomic force microscope (AFM) (NanoWizard, JPK, Berlin, Germany) as previously reported [121]. Firstly, AFM tips (CS38/No Al, µmasch, Sofia, Bulgaria) and glass slides (Thermo Fisher Scientific) were cleaned by piranha solution (70%v/v H_2SO4, 30% H_2O_2) and incubated overnight. Then, the tips and glass slides was cleaned with 1mL ultrapure water for 5 times, and with PBS for 3 times. Tips and slides were coated with ethoxy silane polyethylene glycol (PEG) acid (Nanocs, New York, USA) and incubated for 1h at room temperature. After cleaning with PBS 3 times, recombinant VLA4 (R&D systems, Minneapolis, USA), or anti-vWF antibodies (DAKO GmbH, Jena, Germany) were subsequently coupled to AFM tips via PEG linker. VCAM1 (R&D systems, Minneapolis, USA) was coupled to glass slides via PEG linker.

Recombinant human wild type vWF and 1000 U/mL unfractionated heparin (Merck, Darmstadt, Germany) (1 mg/mL in PBS) formed complexes and attached to the AFM tip via the anti-vWF antibody. The AFM tip was approached to the glass slide. The interaction experiments were performed at different nominal loading rates (5,000 - 160,000 pN/s) and the rupture forces were recorded. At least 500 force curves per loading rate have been analyzed. The onset of repulsion was determined by fitting force-distance curve with the Hertz model as previously reported[122]. Schematic drawing was shown in Figure 4.

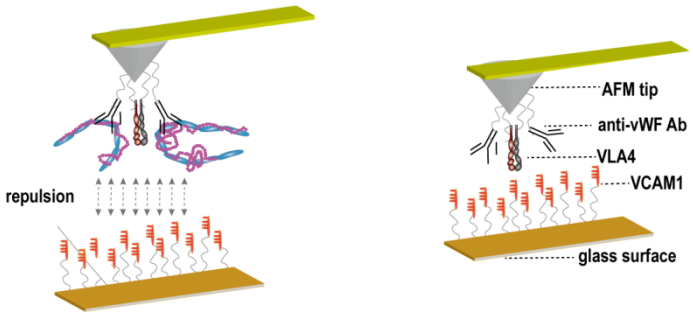

Figure 4. Schematic drawing of SMFS experiments.

Recombinant VCAM1 and VLA4 were covalently linked to glass slides or AFM tips, respectively. A preformed complex of vWF and HS was attached to the tip via a covalently

linked vWF antibody. Then, the functionalized tip was approached to the surface and the force required to contact the surface was recorded. Adapted from **Wang, Y.** *et al.*, 2022[17].

2.2.20 Gel chromatography

The molecular weight of proteoglycans was studied by gel chromatography. The genetically engineered cells were cultured and incubated with 200 µCi/mL ^{35}S-sulfate (Perkin Elmer) for 24h to metabolically label proteoglycans with ^{35}S radioisotopes. After washing with PBS three times, cells were digested with trypsin (1 mg/mL) for 5 min at 37°C. The free glycosaminoglycan chains which derived from cell surface or matrix proteoglycans were purified from the trypsin fraction as described previously[123]. Nitrous acid was used to degrade HS at pH 1.5 with 0.5 M HNO_2[124]. Chondroitinase ABC (Seikagaku) was used to degrade CS at pH 8.0 with 50 mM Tris-HCl, 30 mM Na-acetate in 0.1 mg/mL BSA. Gel chromatography was performed on superose 6 HR10/30 column (Amersham Biosciences). NH_4HCO_3 (0.5 M) was used for elution. The carbohydrate chain fractions were collected at 1-min intervals. The radioactivity was monitored by liquid scintillation counting. Heparin (8.3 kDa) and hyaluronan (19, 30, 43 and 210 kDa) were used for standards.

2.2.21 Surface acoustic wave (SAW) biosensor

SAW measurements were performed to measure the interaction between vWF and VLA4 (R&D systems, Minneapolis, USA) using a Sam5 Blue SAW biosensor (SAW Instruments GmbH, Munich, Germany). For preparing a VLA-4 containing model membrane at the sensor surface, a model membrane consisting of 20 mol % DGS-NTA (Ni) and 80 mol % DPPC (Sigma- Aldrich) was formed using the Langmuir−Blodgett technique and transferred to the sensors, as described before[125]. Prior to the experiment, 10min baseline equilibration with a buffer flow (40 µL/min) was performed. Then, 2 µg recombinant human His-tagged VLA4 was injected with a flow rate of 20 µL/min for binding of the His-tag to the DGS-NTA (Ni) lipid in the membrane. Next, a dilution series vWF from 0.85 nM to 137 nM in running buffer (1 mM $CaCl_2$, 1 mM $MgCl_2$, 0.5 mM $MnCl_2$) was injected for the VLA4 binding measurements. Dissociation constant (K_D) values were extracted from the binding curves using the SamBlue FitMaster software.

2.2.22 Statistics

Statistical analysis was performed with GraphPad Prism 6 software and significance was tested by Student's t-test. All results are presented as means ± SD as indicated in the legend. $P < 0.05$ was considered as significant difference.

3 Results

3.1 Plasmatic vWF encircles blood flowing melanoma cells.

To prove that blood flowing melanoma cells can interact with plasmatic vWF, human melanoma MV3 cells were first stained with a green fluorescent dye, then spiked into human hirudinized whole blood. After incubation at 37°C for 30min, the “buffy coat” was isolated containing leukocytes and MV3 cells. Figure 5A, B showed that MV3 cells accumulated plasmatic vWF at their surface. What is more, no vWF-related fluorescence signal was found at the surface of leukocytes indicating a highly specificity binding of the plasmatic vWF to the melanoma cell surface.

Because previous reasearch suggested that cell surface attached HS was a relevant binding partner for vWF[116], the impact of melanoma cell exposed HS on vWF binding was further investigated. Three melanoma cell lines that expose different levels of HS were selected. Immunofluorescence staining and flow cytometry indicated that the human melanoma cell line MV3 expressed highest HS levels. Lowest HS expression was found in the murine melanoma cell line B16F10, whereas the human IGR37 melanoma cells produced moderate amounts of HS (Figure 5C, D). Figure 5 E, F shows that the binding of vWF to the cellular surface was in direct proportion to the HS levels.

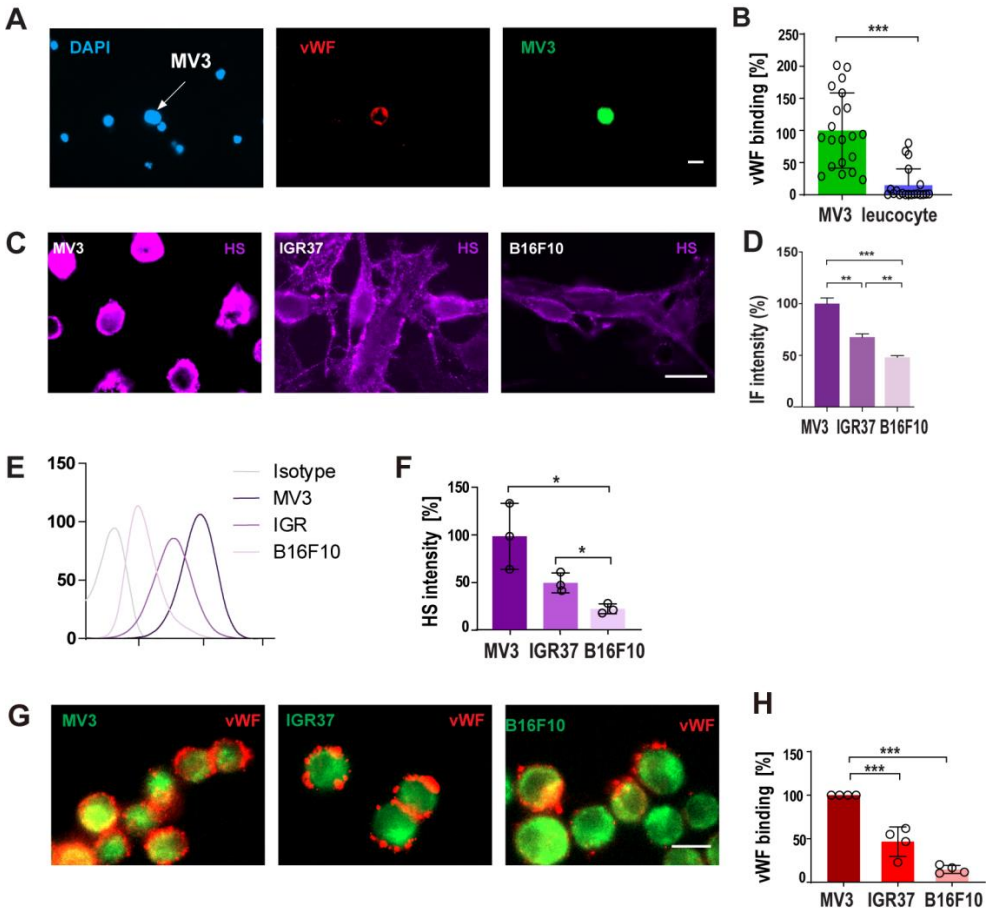

Figure 5. Different melanoma cells have distinct vWF binding capacities.

(A) Fluorescence labeled human melanoma MV3 cells spiked with whole human hirudinised blood. Only MV3 cells (green) can interact with plasmatic vWF (red). (B) Quantification of vWF binding indicate that plasmatic vWF was able to specifically recognize MV3 cells (n = 20). (C) Fluorescence images showing the expression of HS on different melanoma cell lines MV3, IGR37 and B16F10. (D) Quantification of HS expression on MV3, IGR37 and B16F10 by Image J (n = 10). (E) Verification of melanoma cell related HS expression by flow cytometry. (F) Quantification of HS expression in D (n = 3). (G) Fluorescence images showing the accumulating of vWF on the surface of MV3, IGR37 and B16F10 cells. (H) Quantification of vWF accumulating on MV3, IGR37 and B16F10 cells by on-cell ELISA (n = 4). Scale bars = 10 µm. Fluorescence images were taken with a Zeiss Observer.Z1 operated by Zen software and equipped with an Axiocam MRm camera. The applied 40x oil objective had a numerical aperture of 1.3. Data are presented as the mean ± SD, **P*< 0.05, ***P*< 0.005, ****P*< 0.0005. Adapted from **Wang, Y.** *et al.*, 2022[17].

3.2 The expression level of integrins did not correlate with vWF binding capability.

To clarify the role of integrins and in particular of β_3 integrins in vWF binding, first, their protein level in the three selected melanoma cell lines were measured by immunofluorescence staining (Figure 6A). Integrin β_3 was scarcely expressed in MV3 cells (Figure 6A, left), which have the strongest capacity of binding with vWF. B16F10 cells have moderate integrin β_3 expression (Figure 6A, right). However, IGR37 cells, which have a the highest integrin β_3 expression, bind moderate amount of vWF. Further, mRNA level expression of α_V β_3 and the related β_5 was measured by qPCR (Figure 6B). Although all three cell lines expressed considerable amounts of $\alpha_V\beta_3$ integrins, the expression levels did not correlate with the vWF binding capability, suggesting that at least integrins do not play the major role in the binding of vWF to melanoma cells.

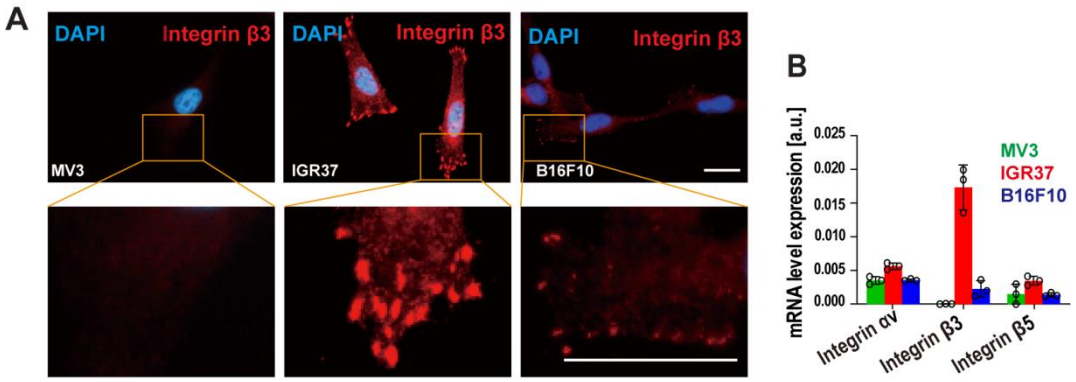

Figure 6. The protein level and mRNA level of integrins expression.

(A) Fluorescence images showing the protein level of Integrin β3 expression on MV3, IGR37 and B16F10 cells. (B) The mRNA expression of integrin α_V β_3 and β_5 in MV3, IGR37 and B16F10 cells melanoma cell lines was measured by qPCR (n = 3). Scale bars = 10 µm. Fluorescence images were taken with a Zeiss Observer.Z1 operated by Zen software and equipped with an Axiocam MRm camera. The applied 40x oil objective had a numerical aperture of 1.3. Data are presented as the mean ± SD, **P*< 0.05, ***P*< 0.005, ****P*< 0.0005. Adapted from **Wang, Y.** *et al.*, 2022[17].

3.3 Binding of vWF to melanoma cell surface mainly depends on HS.

To better understand the molecular mechanism of the vWF accumulating on melanoma cell surface, the capability of melanoma MV3 cells to interact with different recombinant vWF mutants was compared. Previous researchers showed cell surface HS and integrins might be binding partners for vWF. So, vWF lacking the A1 domain and thus the binding site for HS and vWF lacking the RGD-motif, the binding site for $\alpha_V\beta_3$ integrins were included (Figure 7A). Compared with wt vWF (Figure 7B, left), lack of the A1 domain (Figure 7B, middle) reduced the binding of vWF to the MV3 cell surface pointing towards the involvement of HS. Also, the lack of the RGD-motif (Figure 7B, right) attenuated vWF binding. However, the effect was less pronounced (Figure 7B, C).

Further experiments using tinzaparin and cilengitide were also applied to study the molecule mechanism involved in the binding of vWF to melanoma cells. Tinzaparin is a low-molecular weight heparin and thus a close molecular relative of HS which could block the binding of vWF to melanoma cell surface HS. Cilengitide mimics the RGD-motif and is therefore could inhibit the binding of vWF to $\alpha_V\beta_3$ integrins.[126] In agreement to the experiments with the vWF mutants, interference of the vWF binding by tinzaparin further suggested that HS contributes strongly to vWF accumulation at the cellular surface (Figure 7D, E). In comparison, inhibition of integrins by cilengitide prevented the binding of vWF less efficiently. Taken together these data suggested that the main driver of the interaction between melanoma cells and vWF is HS and the A1 domain of vWF.

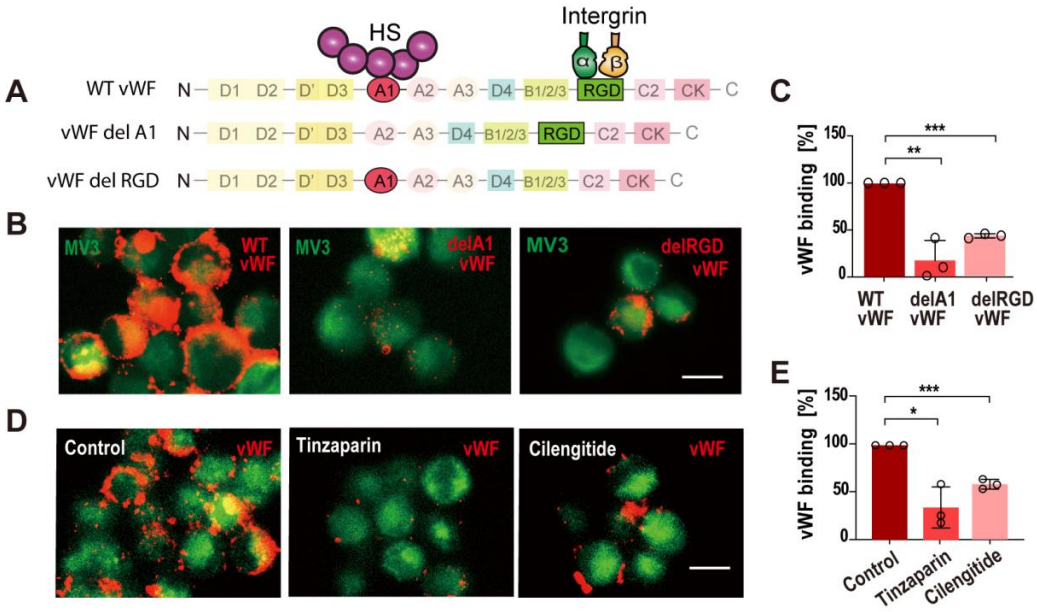

Figure 7. Binding of vWF to melanoma cells depends on HS.

(A) Schematic painting of WT vWF and different vWF mutants: vWF lacking the A1 domain, and vWF lacking the RGD-motif. Integrins bind to vWF RGD motif, HS binds to vWF A1 domain. (B) The binding of vWF to MV3 cells was attenuated by using vWF mutants lacking of the A1 domain or the RGD motif. (C) Quantification of vWF binding by on-cell ELISA indicated that binding of vWF depended mainly on the A1 domain (n = 3). (D) The binding of vWF to MV3 cells was attenuated by Cilengtide and Tinzaparin. Tinzaparin competitively binds to A1 domain. Cilengitide is an inhibitor of $\alpha_V\beta_3$ integrin. (E) Quantification of vWF binding by on-cell ELISA confirmed that the binding of vWF to the cell surface was mainly mediated by the interaction with the A1 domain (n = 3). Fluorescence images were taken with a Zeiss Observer.Z1 operated by Zen software and equipped with an Axiocam MRm camera. The applied 40x oil objective had a numerical aperture of 1.3. Scale bars=10 µm. Data are presented as the mean ± SD, **P*< 0.05, ***P*< 0.005, ****P*< 0.0005. Adapted from **Wang, Y.** *et al.*, 2022[17].

3.4 HS is the most dominant glycan on the melanoma cell surface.

Although the involvement of HS in the binding of vWF to melanoma cells was showed by the preceding experiments, the contribution of other glycocalyx at the cellular surface such HA or CS cannot be excluded (Figure 8A). Therefore, the mRNA level of enzymes involved in the biosynthesis and presentation of HS, HA and CS was measured by qPCR (Figure 8B). MV3 cells express highly amount of HS-related proteins and enzymes. Especially high expression levels of EXT1 and EXT2 which are key enzymes involved in HS production suggesting a strong abundance of HS. In contrast, mRNAs expression of enzymes, which are related to the synthesis of HA and CS were only slightly expressed. These data suggest that HS is the most dominant glycan on the melanoma cell surface. To further verify this finding, HS (10E4) direct antibody and wheat germ agglutinin (WGA) were used to co-staining MV3 cells. In contrast to the HS-directed antibody, WGA could recognize N-acetyl-glucosamine which means HS, HA, CS and N-linked glycans could all be stained. With fluorescence microscopy, MV3 cells showed a strong co-localization of the WGA and HS staining and comparable fluorescence intensity (Figure 8C). Comparable fluorescence intensity of WGA and HS was also confirmed with flow cytometry (Figure 8D). These data give further evidence that HS is the major glycan on the surface of MV3 cells.

To further underpin these findings and to confirm that HS is crucially involved in the binding of plasmatic vWF to the melanoma cell surface, but not other glycocalyx. MV3 cells were treated with different GAGs degrading enzymes: heparinase to remove HS, hyaluronidase to remove HA and chrondoitinase to remove CS (Figure 8E). After enzymatic removal of HS by heparinase, melanoma cells bound 45 ± 3.3% less vWF, whereas treatment with hyaluronidase and chrondoitinase attenuated vWF binding only by 23 ± 6.9 % and 12 ± 7.2 %, respectively (Figure 8F). Taken together, these data indicate that HS is the most prominent binding partner of vWF on the surface of melanoma cells.

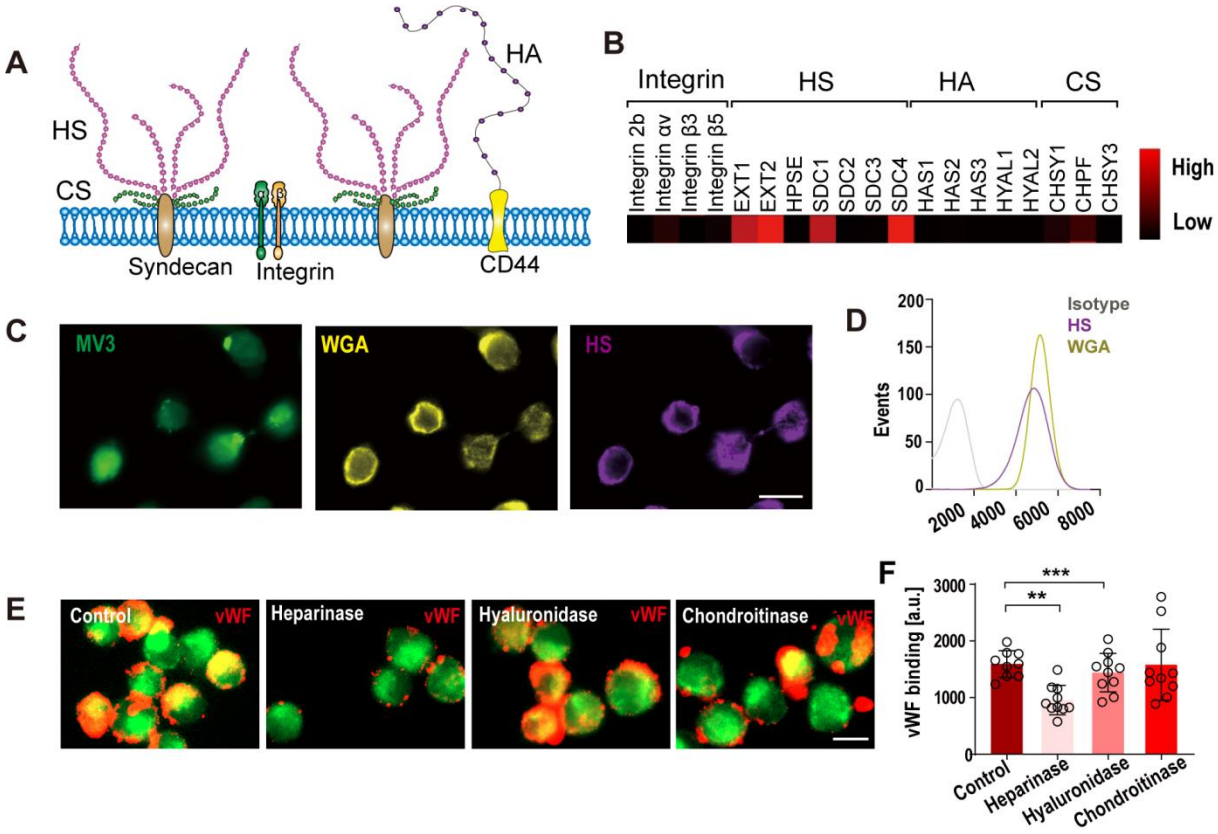

Figure 8. Glycosaminalglycans expressed on melanoma cell surface.

(A) Schematic painting of integrins and different glycocalyx on cell surface. HS and CS chains are covalently linked to SDCs. HA is non-covalently attached to CD44. (B) Transcription levels of integrins and glycocalyx related proteins and enzymes in MV3 cells. Heparanase (HPSE), Hyaluronan Synthase (HAS), Hyaluronidase (HYAL), Chondroitin sulfate synthase (CHSY), Chondroitin sulfate synthase 2 (CHPF). (C) Fluorescence images showing the co-locolization of HS and WGA on the surface of MV3 cells. (D) Flow cytometry showing the comparable fluorescence intensity of HS and WGA on MV3 cells. (E) The binding of vWF on MV3 cell surface after enzymatic treatment of HS (heparinase), HA (hyaluronidase) and CS (chondroitinase). (F) Quantification of vWF binding by fluorescence microscopy indicating HS is the most prominent binding partner of vWF (n = 10). Fluorescence images were taken with a Zeiss Observer.Z1 operated by Zen software and equipped with an Axiocam MRm camera. The applied 40x oil objective had a numerical aperture of 1.3. Scale bars=10 µm. Data are presented as the mean ± SD, *P< 0.05, **P< 0.005, ***P< 0.0005. Adapted from **Wang, Y.** *et al.*, 2022[17].

3.5 Genetic depletion of EXT1 expression.

To study the biological impact of the HS-vWF interaction for tumor progression, I aimed to disrupt HS biosynthesis in melanoma cells by genetic depletion the expression of EXT1. The biosynthesis of HS involves the consecutive action of 11 different enzymes[18]. After its initiation at the protein backbone of the proteoglycan, the chain of HS is elongated by the action of two polymerases EXT1 and EXT2 (Figure 9A). Previously it was shown that the lack of EXT1 is sufficient to fully suppress the HS biosynthesis. ShRNA was used to attenuate the expression of EXT1 in MV3 cells (Figure 9B). Four shRNAs directed against EXT1 were designed and tested in MV3 cells (MV3 shEXT1A-D). A non-specific shRNA was used as a control (MV3 shCTL). Quantitative measurements by qPCR showed that three of the four shRNAs were effective to silence EXT1 expression by at least 78% (Figure 9B). MV3 cells expressing shEXT1A were used in the following experiments.

Moreover, to enable syngenic animal experiments, murine melanoma cell line B16F10 was used. *Ext1* was targeted by CRISPR/Cas9 in B16F10 cells (B16F10$^{Ext1-/-}$) (Figure 9C). A sgRNAs was designed to target exon 1 of the murine EXT1 gene. Sequencing results showed that two kinds of mutation were generated, one with only one base deletion near protospacer adjacent motif (PAM) sequence and the other with a 409 base deletion include the PAM sequence. For the following experiments, B16F10$^{Ext1-/-}$ with 409 base deletion was used.

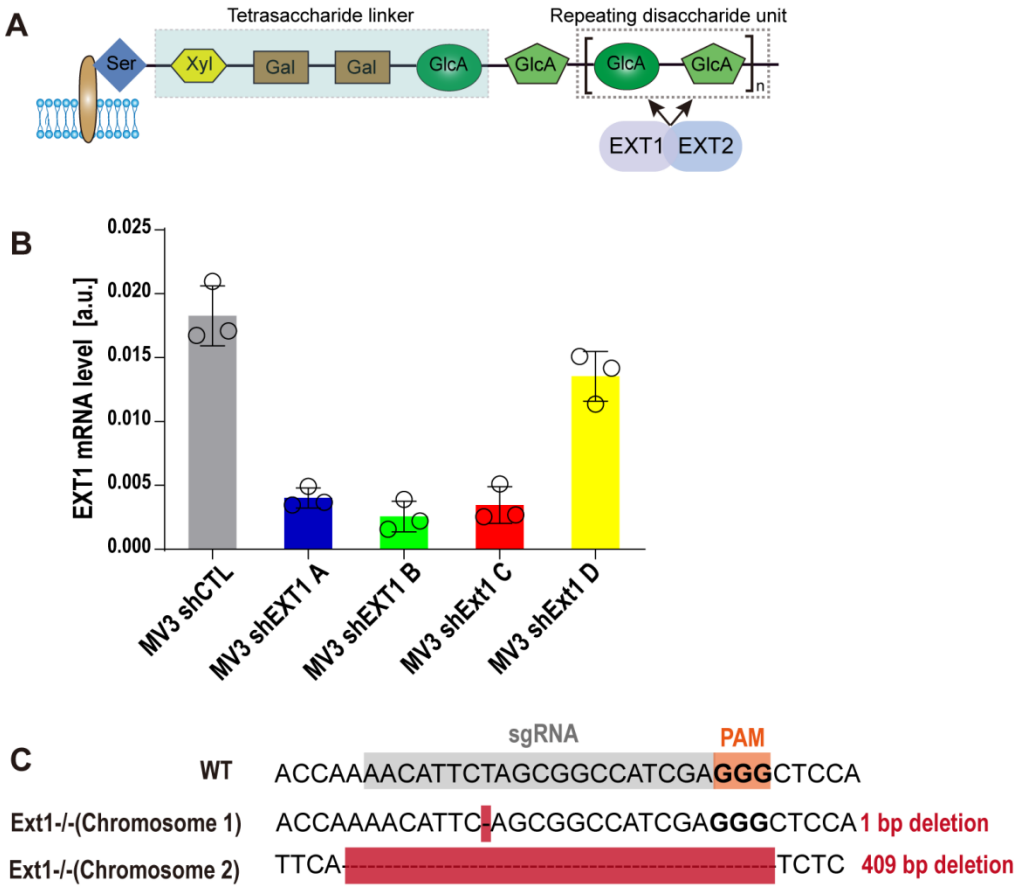

Figure 9. Genetic depletion of EXT1 in MV3 and B16F10 cells.

(A) Assembly of the GAGosome within the Golgi apparatus. After the tetrasaccharidic linker region is coupled, EXT1 and EXT2 are responsible for the subsequent elongation of HS. (B) Transcription level of EXT1 in MV3 control cells (shCTL) and MV3 cells with a silenced EXT1 (shEXT1 A-D) measured by qPCR (n = 3). For the following experiments, MV3 cell transfected with shEXT1 A vector was used, and named as MV3 shEXT1. (C) Knockout of *Ext1* in the mouse melanoma cell line B16F10 by CRISPR/Cas9, sgRNAs was designed to target gene Exon1. A 409bp deletion and 1bp deletion were generated in B16F10 cells individually. B16F10$^{Ext1-/-}$ with 409 base deletion was used for the following experiments. Adapted from **Wang, Y.** *et al.*, 2022[17].

3.6 Genetic depletion of EXT1 abrogated HS biosynthesis

To determine whether genetic depletion of EXT1 gene disrupts HS biosynthesis, the expression of HS on the surface of genetically engineered MV3 and B16F10 cells were shown first by immunofluorescence images staining with HS antibody (Figure 10A, D). Compared with MV3 shCTL control cells, the weak fluorescence on MV3 shEXT1 cells suggested HS expressed was largely reduced. There was nearly no HS signal detectable on B16F10$^{EXT1-/-}$ cells. Further, flow cytometry was also used to confirm the abundance of HS expression (Figure 10B, E). MV3 shEXT1 cells exposed 78 ± 6.8% less HS on their surface than MV3 shCTL control cells (Figure 10C). Consistent with immunofluorescence images, CRISPR/Cas9 editing of EXT1 gene abolished HS production on B16F10$^{EXT1-/-}$ cells (Figure 10F).

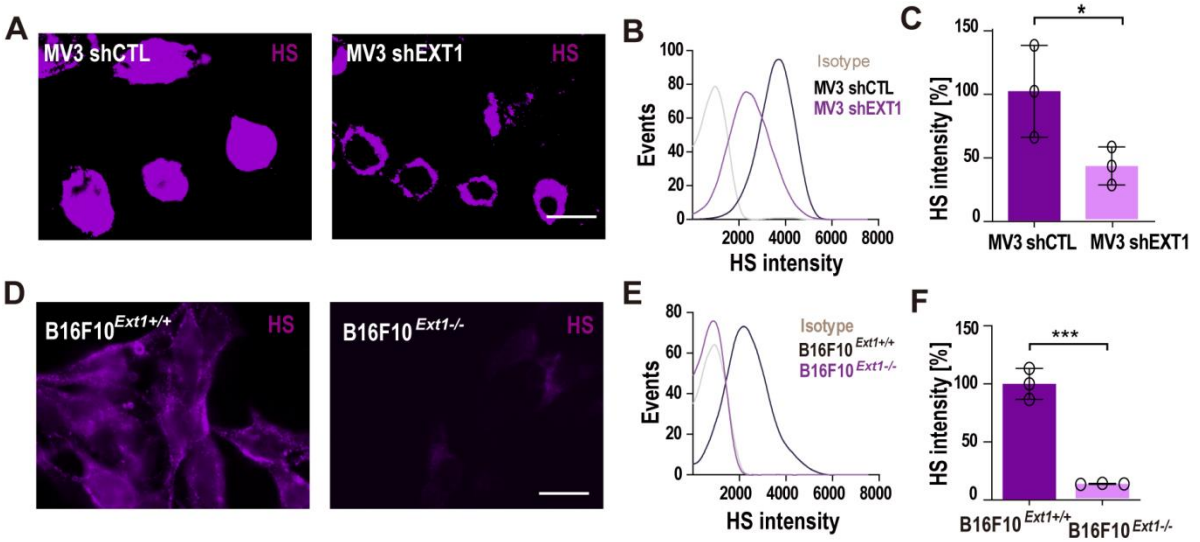

Figure 10. HS synthesis was disrupted by genetic depletion of EXT1.

(A) Immunofluorescence images showing MV3 cells with a silenced EXT1 expression (shEXT1) reduced the amount of HS at the cell surface. (B) HS expression on MV3 shCTL and shEXT1 cells measured by flow cytometry. (C) Quantification of HS expression as measured by flow cytometry confirmed that the expression of HS on MV3 shEXT1 cell was largely reduced (n = 3). (D) Immunofluorescence images showing nearly no HS expressed on B16F10 cells with a CRISPR/Cas9 mediated Ext1 knockout (*Ext1*$^{-/-}$). Fluorescence images were taken

with a Zeiss Observer.Z1 operated by Zen software and equipped with an Axiocam MRm camera. The applied 40x oil objective had a numerical aperture of 1.3. Scale bars = 10 µm. (E) HS expression on B16F10 cells measured by flow cytometry. (F) Quantification of HS expression as measured by flow cytometry confirmed that B16F10$^{EXT1-/-}$ cells were completely deficient in HS (n =3). Data are presented as the mean ± SD, *P< 0.05, **P< 0.005, ***P< 0.0005. Adapted from **Wang, Y.** *et al.*, 2022[17].

3.7 Molecular weight of proteoglycans in the genetically engineering cells.

To obtain a more profound characterization of the engineered cells, the proteoglycan-exposed carbohydrates were isolated. Cells were first incubated with ^{35}S-sulfate for 24h. Then the metabolically label proteoglycans including HS and CS chains were isolated, and the molecular weight was studied by gel chromatography (Figure 11A - F). The ^{35}S-labeled HS chains produced by shRNA silenced MV3 were shorter than those of control transfected cells (Figure 11B). And comparing the standard polysaccharides, the overall size of carbohydrate chains can be estimated. The molecular weight of the HS chains exposed by MV3 shCTL cells were between 43kDa and 210kDa, while MV3 shEXT1 cells produced chains with a molecular weight between 30kDa and 43kDa (Figure 11B). The molecular weight of the CS chains was not affected in shEXT1 cells (Figure 11C). In agreement with the flow cytometry data, CRISPR/Cas 9 knockout of *Ext1* in B16F10 cells resulted in complete absence of ^{35}S-labeled HS chains, while the molecular weight of HS in B16F10 cells was about 43kDa. (Figure 11E). The molecular weight of the CS chains remained almost unaffected in B16F10$^{EXT1-/-}$ cells (Figure 11F), suggesting that the knockdown EXT1 can be solely attributed to the changes in HS expression (Fig. 11D).

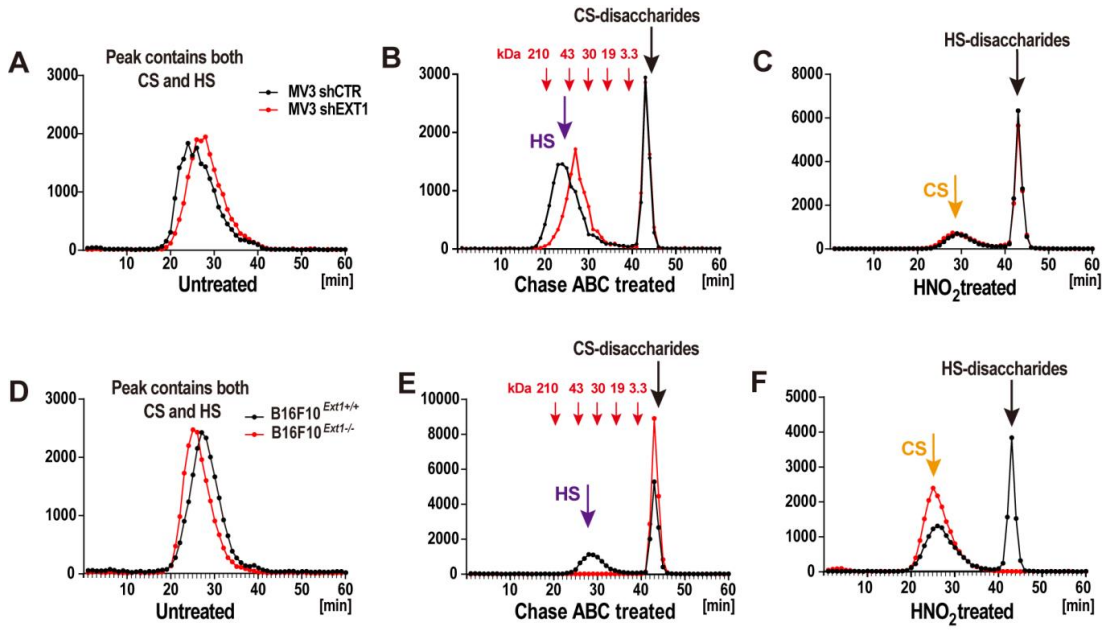

Figure 11. The molecular weight of the HS and CS proteoglycan measured by gel chromatography.

(A) MV3 shCTL or shEXT1 cells without enzymatic treatment showing peak with both HS and CS proteoglycans (B) MV3 shCTL cells produced HS with a molecular weight between 43kDa and 210kDa. While MV3 shEXT1 cells produced shorter HS chains between 30kDa and 43kDa. (C) The molecular weight of CS chains in MV3 shCTL and MV3 shEXT1 cells was the same suggesting knocking down EXT1 does not affect CS expression. (D) B16F10 *Ext1*$^{+/+}$or *Ext1*$^{-/-}$ cells without enzymatic treatment showing peak with both HS and CS proteoglycans (E) B16F10 *Ext1*$^{+/+}$ cells produced HS with a molecular weight of about 43kDa, whereas after *Ext1* knockout, B16F10 *Ext1*$^{-/-}$ cells produced no HS. (F) The molecular weight of CS chains remained almost unaffected in B16F10$^{EXT1-/-}$ cells. Data are presented as the mean ± SD, *P< 0.05, **P< 0.005, ***P< 0.0005. The data were produced by Prof. Dr. Marion Kusche-Gullberg. Adapted from **Wang, Y.** *et al.*, 2022[17].

3.8 The density of HS on melanoma cell surface was not effected by genetically depletion EXT1.

Next, to better understand the nanoscaled morphologies of the proteoglycan on cell surface, the STED microscopy was applied to measure the proteoglycan density at the surface of the melanoma cells. Clusters on cell membrane present heparan sulfate proteoglycans (Squire, J. M.2001) with interstitial gaps in the hundred nanometer range (Weinbaum, S,2003. Kabedev, A,2018). In line with this concept, the magnified image clearly showed cell membrane HS clusters (Figure 12A-D). The weaker fluorescence signal of cells reflect the comparable low expression of HS synthesis (Figure 12B, D) which present on the images as smaller cluster size. Of note, lack of EXT1 reduced proteoglycan size, but not their density. MV3 cells exposed HS proteoglycans with an average distance of 220nm. The average distance of HS clusters on B16F10 cells was smaller, approximately 180 nm. (Figure 12E, F).

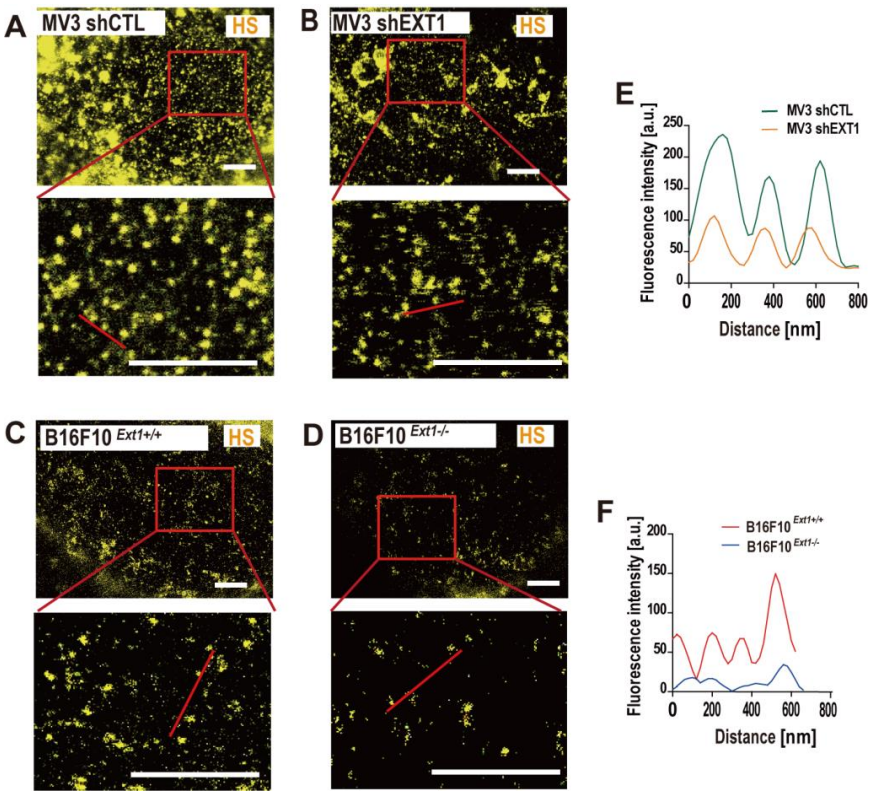

Figure 12. Characterization the density of HS on melanoma cell surface.

(A, B) Nanometric HS distributions on the surface of MV3 cells measured by STED microscopy. Compared with MV3 shCTL cells, MV3 shEXT1 cells produced smaller HS clusters.

(C, D) HS distributions on the surface of B16F10 cells. Scale bars = 2 µm. (E, F) Distance of HS clusters on the membrane of MV3 and B16F10 cells analyzed with STED images. The average distance between the HS proteoglycan was approximately 220 nm for MV3 cells and 180 nm for B16F10 cells. Adapted from **Wang, Y.** *et al.*, 2022[17].

3.9 Characterization of the HS chain length at the melanoma cell surface.

Recently, a NP-based titration method was established to determine the length of cell surface exposed glycans.[20] Accordingly, the average contour length of the HS chain were calculated by measuring the binding of NP to cell surface exposed HS (Figure 13A). The HS chain length of MV3shCTL cells was 240 ± 14.5 nm, whereas MV3shEXT1 cells exposed chains with a length of 61 ± 2.0 nm. B16F10$^{EXT1+/+}$ cells were characterized by a HS chain length of 131 ± 1.7 nm, B16F10$^{EXT1-/-}$ cells exposed no HS chains (Figure 13B). In solution, HS behave like a worm-like chain with a persistence length of 2.08 nm which was previously determined by small-angle x-ray scattering [127]. Accordingly, HS exhibits a bush-like conformation at the cellular surface[20] and the radius of the coiled HS chain (radius of gyration, R_G) at the surface of the melanoma cells were 10 ± 0.1 nm (B16F10 cells) and 13 ± 0.1 nm (MV3).

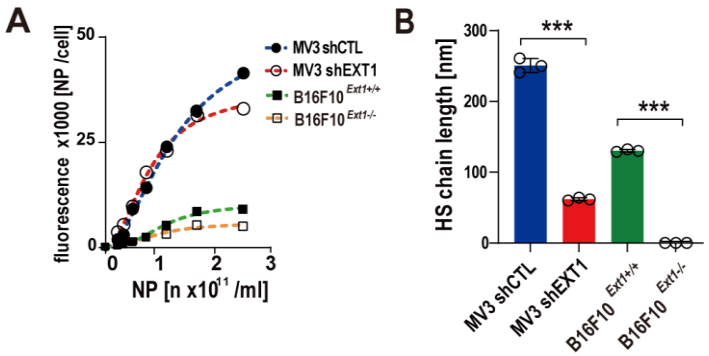

Figure 13. Characterization the length of the melanoma cell HS

(A) Flow cytometry showed the binding of nanoparticle (NP) to MV3 and B16F10 cells is dose-dependent. (B) The length of HS chain was calculated based on STED images and NP

titration. MV3shCTL and MV3shEXT1 cells produced HS with a length of 240 ± 14.5 nm and 61 ± 2.0 nm respectively. Whereas B16F10$^{EXT1+/+}$ cells exposed chains with a length of 131 ± 1.7 nm and B16F10$^{EXT1-/-}$ cells produced no HS. (n=3) Data are presented as the mean ± SD, *P< 0.05, **P< 0.005, ***P< 0.0005. Adapted from **Wang, Y.** *et al.*, 2022[17].

3.10 Loss of HS attenuated binding of vWF to the melanoma cell surface

In the next set of experiments, the binding of vWF to the genetically engineered melanoma cells was analyzed. In agreement with the hypothesis that HS is a main interaction partner of vWF, a strongly reduced vWF binding upon EXT1 knockdown or knockout to the surface of melanoma cell was shown in Figure 14A, C. The vWF binding ability was further verified by ELISA-like assay, which showed consistent results with immunofluorescence staining (Figure 14B, D). Figure 14E showed that the binding of vWF to cell surface was in a linear manner dependent on HS chain length.

To exclude that potential off-targets of the CRIPSR/Cas9 approach contribute to the attenuated vWF binding, the B16F10$^{Ext1-/-}$ cells were rescued by re-expression of EXT1 (B16F10$^{Ext1-/-;Ext1+}$). The reoccurrence of HS expression at the cell surface was detected by flow cytometry (Figure 14F). Moreover, figure 14G shows a significant rescue of vWF binding after *Ext1* re-expression. In further control experiments, another key enzyme involved in HS prolongation: Ext2 was also being knocked out in B16F10 cells. Figure 14H showed no HS expression by Ext2 knockout cells, and thus abolished vWF binding (Figure 14I).

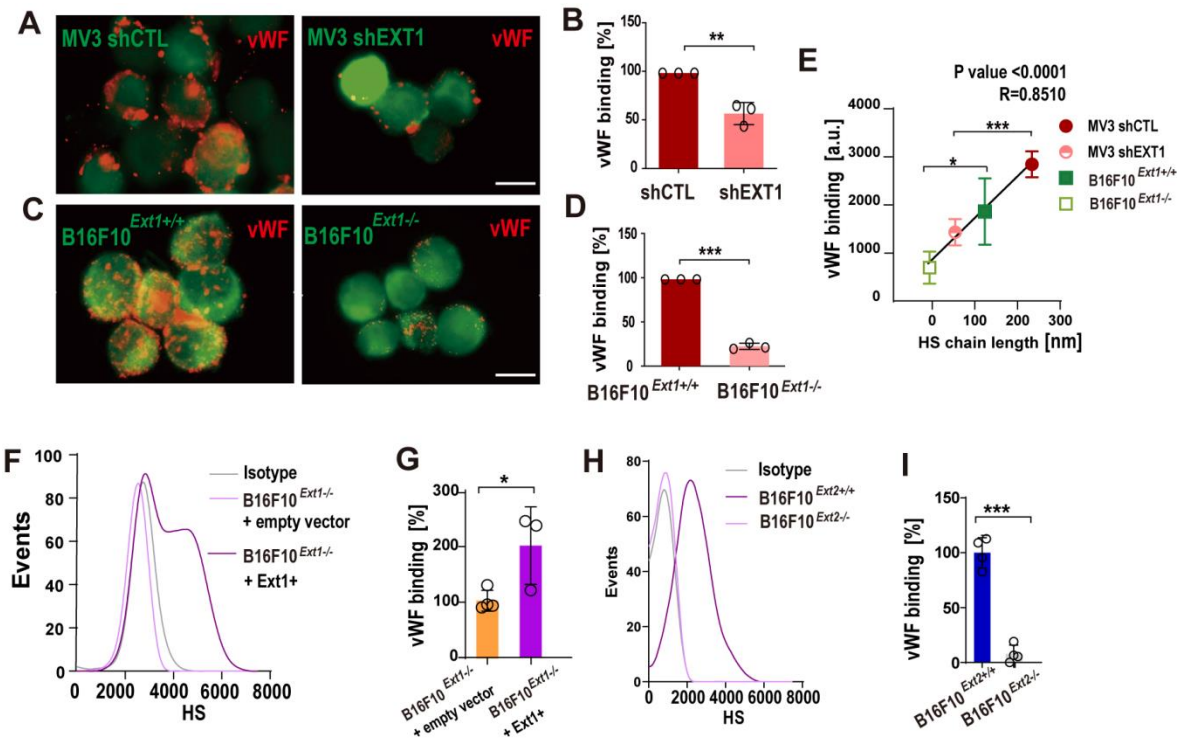

Figure 14. Binding of vWF to melanoma cells was attenuated by loss of HS.

(A) Compared with MV3shCTL cells, MV3shEXT1 cells with a reduced HS synthesis bound less vWF on the surface. (B) Quantification of vWF binding by on-cell ELISA (n = 3). (C) vWF binding to the surface of B16F10$^{Ext1+/+}$ and B16F10$^{Ext1-/-}$ cells. Less vWF bound to the surface of B16F10$^{Ext1-/-}$ cells (D) Quantification of vWF binding by on-cell ELISA (n = 3). Scale bars = 10 µm. (E) The capacity to bind vWF was linearly dependent on the HS chain length. (F) The HS expression on B16F10$^{Ext1-/-}$ and Ext1 rescued B16F10$^{Ext1-/-}$ cells measured by flow cytometry. Reoccurrence of HS expression was shown after knockin of *Ext1*. (G) On-cell ELISA showed rescued vWF binding to B16F10$^{Ext1-/-}$ + *Ext1* cells. (H) The HS expression on B16F10$^{Ext2+/+}$ and B16F10$^{Ext2-/-}$ cells measured by flow cytometry. Knockout of *Ext2* abolished HS expression. (I) On-cell ELISA showed knockout of *Ext2* abolished vWF binding to B16F10$^{Ext2-/-}$ cells, further confirming that HS is the binding partner of vWF. (n = 4). Data are presented as the mean ± SD, *P< 0.05, **P< 0.005, ***P< 0.0005. Adapted from **Wang, Y.** *et al.*, 2022[17].

3.11 The triangular interaction between HS, integrin and vWF

Previously, it has been shown that cell surface exposed glycosaminoglycans and proteoglycans can support integrin binding[128]. Therefore, the triangular interaction between HS, integrin and vWF was studied in more detail. To this end, the genetically engineered melanoma cells were used to repeat the experiments with the vWF mutants (Figure 15A). To better understand the obtained results, a simple theoretical model was developed. I assumed that HS is able to promote integrin function in an additive manner (Table 1). By feeding the theoretical model with the experimental data (Figure 15A), different contributions to the binding of vWF were calculated, as relative fractions, the directly HS-related impact on vWF binding (α), the HS-independent integrin activity (β) and the HS-dependent integrin activity (γ) (Figure 15B). These calculations indicate that the HS-related vWF binding (α) is more relevant than the integrin-related binding (β and γ). Moreover, in comparison to the HS-independent integrin activity (β), the impact of HS on integrin activity (γ) played a more prominent role.

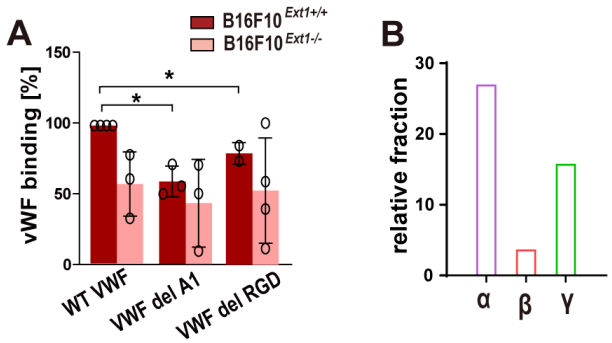

Figure 15. Interaction between HS, integrins, and vWF.

(A) On-cell ELISA showed the binding of different recombinant vWF to B16F10$^{Ext1+/+}$ and B16F10$^{Ext1-/-}$ cells. (n = 3). (B) Based on the data shown in A, the different contributions of HS and integrins to vWF binding were calculated. The binding model distinguished between purely HS dependent vWF binding (α), HS-independent vWF binding to integrins (β) and HS-dependent vWF binding to integrins (γ). Adapted from **Wang, Y.** *et al.*, 2022[17].

	B16F10 EXT1$^{+/+}$	**B16F10 EXT1$^{-/-}$**
wt vWF	A = α+β+γ+b_{wt}	A'= β+b_{wt}
ΔA1 vWF	B = β+γ+b_{A1}	B'= β+b_{A1}
ΔRGD vWF	C = α+b_{RGD}	C'= b_{RGD}

Table 1: Triangular connection between HS, RGD-recognizing integrins and vWF.

The basis of the vWF binding model that used to determine the contribution of HS (α), HS-independent integrin activity (β) and HS-dependent integrin activity (γ). Table organization was calculated corresponding to the data shown in **Figure 15A**. Adapted from **Wang, Y.** *et al.*, 2022[17].

$b_{RGD} = b_{wt}$

β=A'-C';

α=C-C';

γ=B-B'

b_{wt} = background binding of wt vWF

b_{RGD} = background binding of ΔRGD vWF

b_{A1} = background binding of ΔA1 vWF

3.12 HS-mediated enclosure of melanoma cells by vWF attenuated metastasis

To understand the biological relevance of vWF accumulation at the melanoma cell surface *in vivo*, murine melanoma cells B16F10$^{Ext1+/+}$ and B16F10$^{Ext1-/-}$ were injected into the tail vein of

C57BL/6 wild type mice and the formation of macroscopic lung metastasis was analyzed 14 days post inoculation. The results, shown in Figure 16A, indicate that B16F10$^{Ext1-/-}$ formed significantly more metastatic foci than the control cells (B16F10$^{Ext1+/+}$), suggesting that B16F10$^{Ext1-/-}$ cells were more metastatic. To understand whether the binding of vWF to cell surface was responsible for attenuated lung metastasis formation, vWF knockout mice were used. B16F10$^{Ext1+/+}$ and B16F10$^{Ext1-/-}$ cells were injected into the tail vein individually. Figure 16B shows that in vWF deficient mice, B16F10$^{Ext1+/+}$ cells formed as much metastasis as B16F10$^{Ext1-/-}$ cells, indicating that the antimetastatic effect was vWF dependent. Quantitative analyses of the animal experiments are presented in Figure 16C. These results were consistent with previous researches that vWF-/- mouse had increased metastatic foci in lung tissues, and infusion of recombinant vWF can correct the enhanced lung metastasis,[82] clearly indicating the anti-metastatic role of vWF. To determine whether the HS deficiency phenomenon persists *in vivo*, the expression of HS within metastatic foci were evaluated (Figure 16D). Compared to the metastatic foci formed by B16F10$^{Ext1+/+}$ cells, B16F10$^{Ext1-/-}$ cells formed metastatic foci with barely HS expression. Quantitative analyses of the animal experiments are presented in Figure 16E. Taken together, these results suggest that binding of plasmatic vWF to melanoma cells attenuated hematogenous metastasis, whereas melanoma cells lack of HS expression avoids the binding of vWF and thus facilitates metastasis.

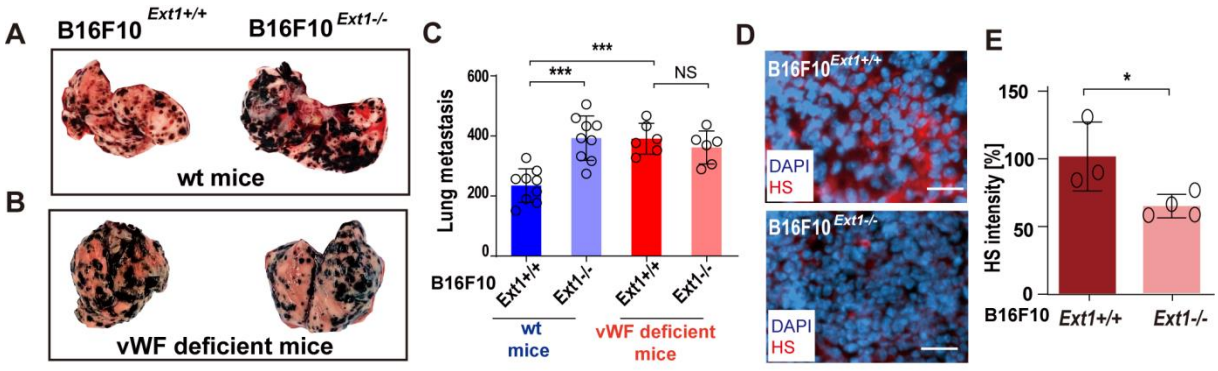

Figure 16. Binding of vWF to melanoma cells reduced lung metastasis.

(A) Representative images of metastatic lungs of wild type (wt) mice. B16F10$^{Ext1-/-}$ cells formed more metastasis. (B) Representative images of metastatic lungs of vWF deficient

mice. B16F10$^{Ext1+/+}$ cells formed as much metastasis as B16F10$^{Ext1-/-}$ cells. (C) Quantitation of metastatic foci (n = 5). (D) Immunofluorescence staining of HS in the metastatic foci of wt mice formed by B16F10$^{Ext1+/+}$ and B16F10$^{Ext1-/-}$ cells. Scale bars = 20 µm. (E) Quantitation of HS expression (n = 5). Adapted from **Wang, Y.** *et al.*, 2022[17].

3.13 HS expression in melanoma patient tissue.

Next to animal models, the samples of primary human melanoma tissues and metastatic foci were also collected. HS expression was measured by immunofluorescence. S100 was used as a marker for melanoma cells. The results showing that melanoma cells within the primary melanoma tissue express 1.75 times more HS than melanoma cells of metastatic foci (Figure 17A). Quantitative analyses of the HS expression level are presented in Figure 17B. Melanoma patient tissue staining suggesting that tumor cells with reduced HS expression were prone to metastasis.

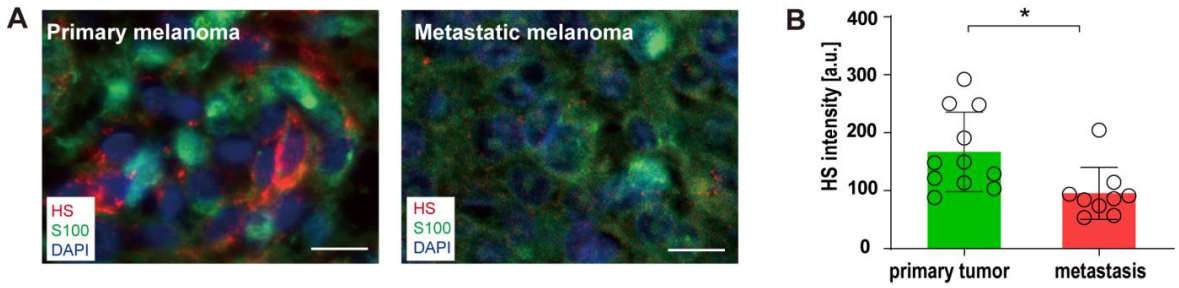

Figure 17. HS expression on primary and metastatic melanoma tissues.

(A) HS expressions on human primary melanoma and metastatic tissues presented by Immune fluorescence staining. S100 serves as a marker for melanoma cells. Scale bars = 20 µm. (B) Quantification of HS expression in patients' primary tumors (n = 11) and metastases (n = 9). Compared to primary tissue, metastatic tissue expresses less HS. Data are presented as the mean ± SD, *P< 0.05, **P< 0.005, ***P< 0.0005. Adapted from **Wang, Y.** *et al.*, 2022[17].

3.14 HS -related genes expression in primary melanomas and melanoma metastases.

Next, the public transcriptome database cBioportal[113, 129] was surveyed to analyse the expression of HS-related genes (EXT1, EXT2, HPSE, SDC1, SDC2, SDC3 and SDC4) in primary melanomas and melanoma metastases (Figure 18A). HPSE is the only mammalian enzyme that can cleave HS. SDCs are the core proteins where HS is anchored. In good agreement with the tissue staining, that melanoma metastatic foci express lower levels of EXT1 and SDC1 compared to primary melanoma. While the mRNA levels of other genes have no significant differences. Then the transcriptome data were also correlated with patients' survival date. Reduced patients' survival was shown with decreased EXT1, SDC2, SDC3, and SDC4 expressions individually. No significant differences were found with EXT1, SDC1 and HPSE. (Figure 18B). Altogether, melanoma cells expressing less HS or the glycoprotein-SDCs were prone to metastasize and thus reduced patients' survival.

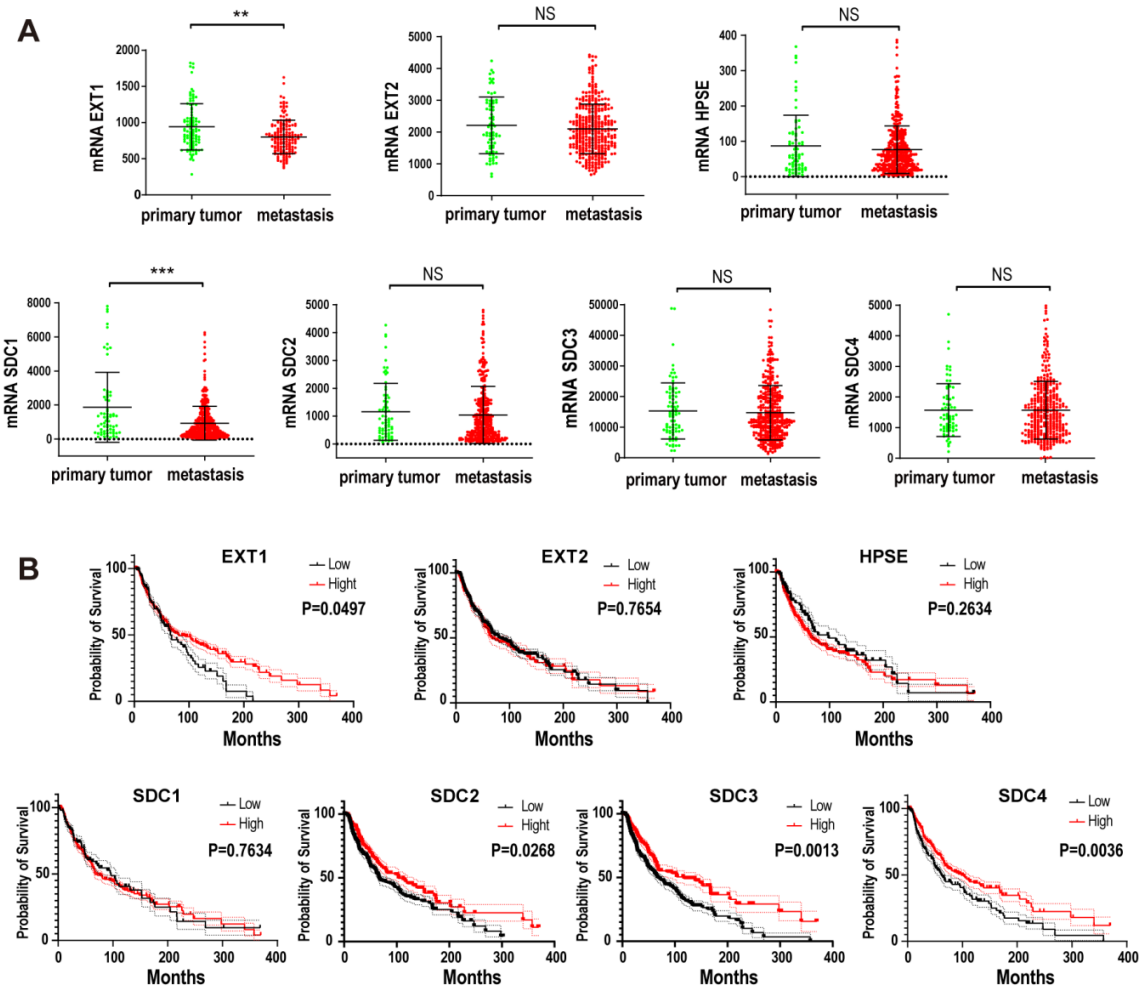

Figure 18 HS -related genes expression in primary melanomas and melanoma metastases.

(A) Transcriptome levels of EXT1, EXT2, HPSE, SDC1, SDC2, SDC3 and SDC4 in melanoma tissues of metastatic foci or primary tumors. Melanoma metastatic tissue expressed less EXT1 and SDC1. Data were obtained from the public transcriptome database cBioportal. (B) Correlation between HS-related genes and melanoma patients' survival was presented as Kaplan-Meier diagram. Reduced EXT1, SDC2, SDC3, and SDC4 expressions were related to reduced patients' survival. Data are presented as the mean ± SD, *P< 0.05, **P< 0.005, ***P< 0.0005. Adapted from **Wang, Y.** *et al.*, 2022[17].

3.15 HS expression in CTCs and the vWF binding ability

Given that plasmatic vWF recognize blood circulating melanoma cells through binding to HS. To further confirm the binding of plasmatic vWF to circulating tumor cell, I aimed to investigate the interaction between vWF and genuine patient-derived CTCs. However, currently no melanoma –patient derived CTCs exist. So, circulating breast cancer cells (CTC-ITB-01) were used. CTC-ITB-01 cells were previously isolated from a metastatic breast cancer patient[30]. Compared to breast cancer cell line MDA-MB-231, circulating breast cancer cell CTC-ITB-01 expressed very low HS (Figure 19A) and thus also binds less vWF (Figure 19B). These data further substantiated that lower HS expression is correlated with the ability of metastasis.

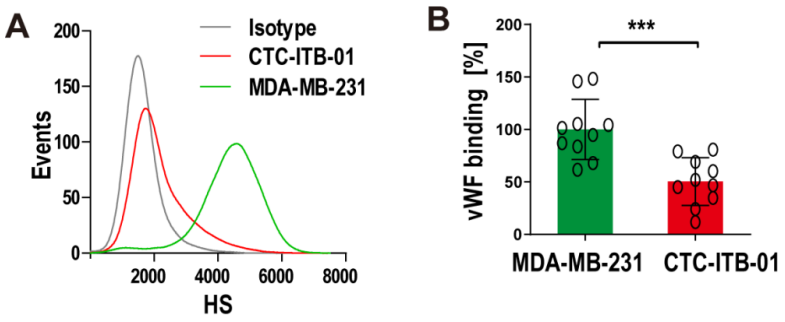

Figure 19. HS expression and vWF binding of breast cancer cells.

(A) HS expression on breast cancer cells measured by flow cytometry. Compared with the breast cancer cell line MDA-MB-231, the circulating breast cancer cell line (CTC-ITB-01) expressed less HS. (B) Quantification of vWF binding capacity measured by fluorescence microscopy (n = 10). Less vWF bound to patient-derived CTC-ITB-01 cells. Data are presented as the mean ± SD, *P< 0.05, **P< 0.005, ***P< 0.0005. Adapted from Wang *et al.*,2022[17].

3.16 vWF attenuated adhesion of cancer cells to the vascular endothelium.

To clarify whether vWF accumulation of cancer cells affected vascular adhesion, microfluidic experiments were performed which were previously used to mimic pathophysiological blood flow conditions and to measure the interaction between tumor cells and the vascular endothelium[116, 130]. HUVECs were seeded on fibronectin-coated microfluidic channels until a confluent layer formed. Prior to the adhesion experiment, HUVECs were stimulated with recombinant TNFα which could induce the expression of adhesion molecules e.g. VCAM1, thus mimicking a tumor-like pro-inflammatory and pro-adhesive microvascular environment. Green fluorescent labeled B16F10$^{Ext1+/+}$ cells and red fluorescent labeled B16F10$^{Ext1-/-}$ cells were perfused simultaneously to the microfluidic channel. The flow experiments were performed at a continuous shear stress of 2 dyn/cm^2 with or without the presence of vWF. Representative snapshots of the flow experiments are shown in Figure 20A. Consistent with the animal experiments, the attachment of B16F10$^{Ext1+/+}$ cells to endothelium was significantly attenuated in the presence of vWF, however, the adhesion of B16F10$^{Ext1-/-}$ cells which can not bind vWF was not affected (Figure 20B). Similar relationships between the vWF binding capacity and the rate of vascular adhesion were also found in microfluidic experiments with human MV3 cells (Figure 20C, D) and patient-derived CTC-ITB-01 (Figure 20E, F). In summary, these data suggested the binding of vWF to cell surface HS prevents vascular adhesion.

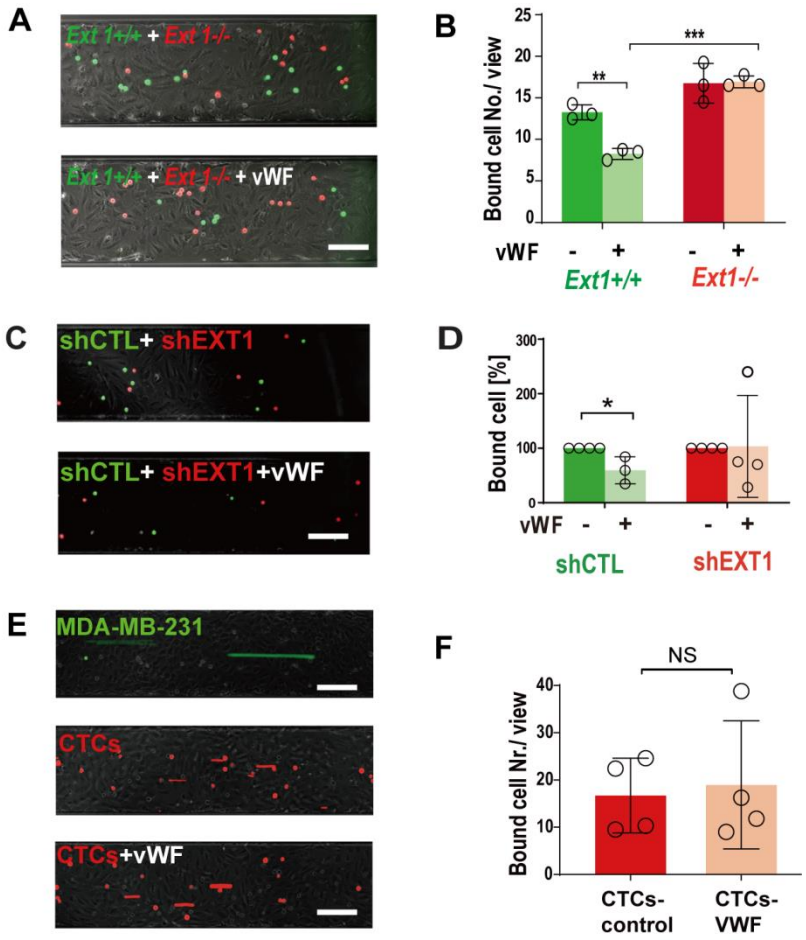

Figure 20. vWF attenuated cells' adhesion to endothelium.

(A) Vascular adhesion of murine melanoma B16F10 cells in the absence or presence of vWF. (B) Quantification of cell adhesion (n = 3). VWF attenuated the adhesion of B16F10 $^{Ext1+/+}$(green) cells but not B16F10 $^{Ext1-/-}$(red) cells. (C) The attachment of human melanoma MV3 cells to HUVECs in the absence or presence of vWF. (D) Quantification of cell adhesion (n = 4). VWF prevented the adhesion of MV3 control cells (shCTL, green) but not of EXT1 knockdown cells (shEXT1, red). (E) Vascular adhesion of MDA-MB-231 cells (green) and CTC-ITB-01 cells (red). VWF can not affect the attachment of CTC-ITB-01 cells. (F) Quantification of cell adhesion (n = 4). bars = 20 µm. Data are presented as the mean ± SD, *P< 0.05. Adapted from **Wang, Y.** *et al.*, 2022[17].

3.17 HS proteoglycan height measurement by ECIS and RICM.

Interestingly, the adhesion rate of melanoma cells was not only affected by vWF (Figure 20A, B). In the absence of vWF, B16F10$^{Ext1-/-}$ cells bound more frequent to the endothelial cell layer than the B16F10$^{Ext1+/+}$ cells. This suggests that the HS layer can attenuate the interaction between the flowing melanoma cells and the endothelium, directly.

ECIS was performed to better understand this HS-related and vWF independent effect. The average space between the adhesive surface and the ventral side of the adhering B16F10 cells was measured. HS deficient B16F10 cells approach closer to the substratum than the corresponding control cells (Figure 21A, B). The calculated distance between the ventral side of the B16F10$^{Ext1+/+}$ cells and the surface was 48.5 ± 15.87 nm, the space underneath the B16F10$^{Ext1-/-}$ cells was only 7.6 ± 4.49 nm. The ECIS measurements suggested that the loss of the HS layer enabled a closer approach of the melanoma cells to the adhesive surface, which in turn can increase the interaction probability of adhesion molecules.

To further verify the ECIS data, RICM was used to determine the distance of the adhering melanoma cells from the substratum at a nanometer resolution. Although distances measured by RICM were higher than the ones determined by ECIS, they were of a comparable magnitude and relation and confirmed that B16F10$^{Ext1-/-}$ cells can approach closer to the adhesive surface than B16F10$^{Ext1+/+}$ cells (Figure 21C, D). Basing on the ECIS and RICM measurements, the contribution of the HS layer to the distance between the adhesive surface and the ventral site of the cells can be calculated (Figure 21E). The calculated distance was in good agreement with the average thickness of the HS layer, which was determined by the nanoparticel titration method (Figure 13C).

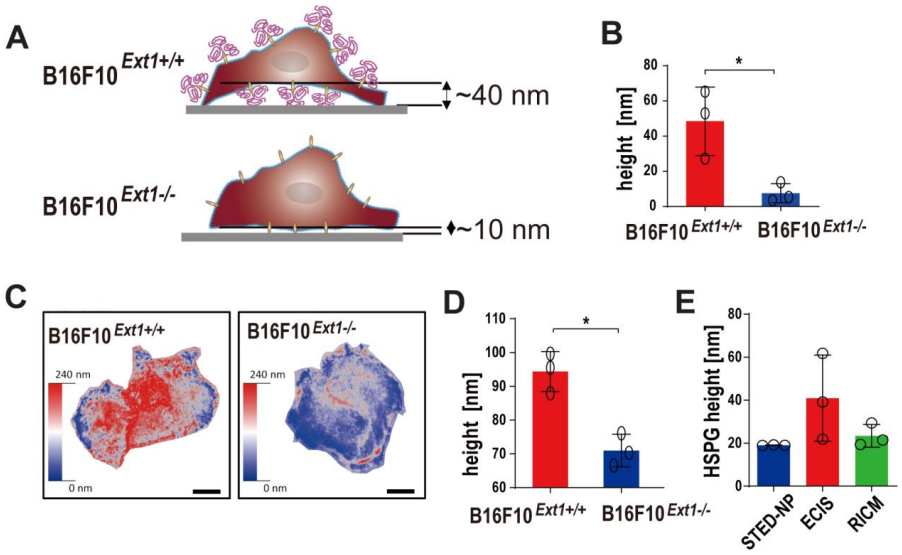

Figure 21. HS proteoglycan height measurements.

(A) Schematic painting of the cell attachment on fibronectin-coated surfaces. The HS layer on the B16F10$^{Ext1+/+}$ cells hinders a tight contact to the substratum (B) The height of B16F10$^{Ext1+/+}$ and B16F10$^{Ext1-/-}$ cells measured by ECIS. (C) RIPM images showed the distance of the adhering B16F10 cells to the substratum. The applied 63x oil objective had a numerical aperture of 1.25. Scale bars = 5 µm. (D) Calculated height of B16F10 by RICM measurements. (E) The heights of HS layer on B16F10$^{Ext1-/-}$ cells were measured by STED/NP titration, ECIS, and RICM. Data are presented as the mean ± SD, *P< 0.05. Adapted from **Wang, Y.** *et al.*, 2022[17].

3.18 The adhesion of B16F10 cells to the endothelium was VCAM1/VLA4 dependent.

In the following experiments, the molecular origin of the antimetastatic effect of vWF was clarified. I assumed that vWF can block adhesion molecules at the surface of the melanoma cells. Accordingly, potential receptors that could mediate the binding of B16F10 cells to endothelial cells was investigated. Previous research reported Thy1, P-selectin and VCAM1 as relevant endothelial adhesion molecules[55, 119, 131]. Thy1 can interact with $\alpha_v\beta_3$ integrins. P-selectin can interact with sialy-lewis-X and low-molecular weight heparins. VCAM1 is the

receptor for VLA4 which is also called $\alpha_4\beta_1$ integrins. Data from qPCR confirmed the expression of $\alpha_4\beta_1$ integrins on B16F10 cells. (Figure 22A). Gene expression analysis by qPCR indicated high mRNA levels of VCAM1 in TNFα stimulated endothelial cells, whereas expressions of Thy1 and P-selectin were below the detection limit (Figure 22B).

Although there was no reasonable expression of Thy1, whether the Thy1/$\alpha_v\beta_3$ integrin interaction contributed to melanoma cell adhesion was tested by microfluidic experiments. Cilengitide was used to block $\alpha_v\beta_3$ integrins and I found that melanoma cell adhesion was not significantly attenuated (Figure 22C, D) suggesting that the Thy1/$\alpha_v\beta_3$ integrin interaction is indeed not relevant in my experimental system.

Moreover, to exclude that P-selectin is able to trap B16F10 cells and that lack of HS may affect P-selectin recognition, static (Figure 22E) and dynamic P-selectin binding assays were performed (Figure 22F). Both assays verify only a minor ability of B16F10 cells to interact with P-selectin under static and dynamic conditions.

Additionally, the contribution of VCAM1 in melanoma cell adhesion was verified by VCAM1 neutralizing antibodies (Figure 22G, H). Blocking of VCAM1 attenuated the attachment of both B16F10$^{Ext1+/+}$ and B16F10$^{Ext1-/-}$ cells to endothelium. Bio5192 was also used to inhibit VLA4, the receptor of VCAM1. Vascular adhesion was abolished in B16F10 cells in the presence of Bio5192. These data indicate that the adhesion of B16F10 cells to the endothelium was mostly VCAM1/VLA4 dependent.

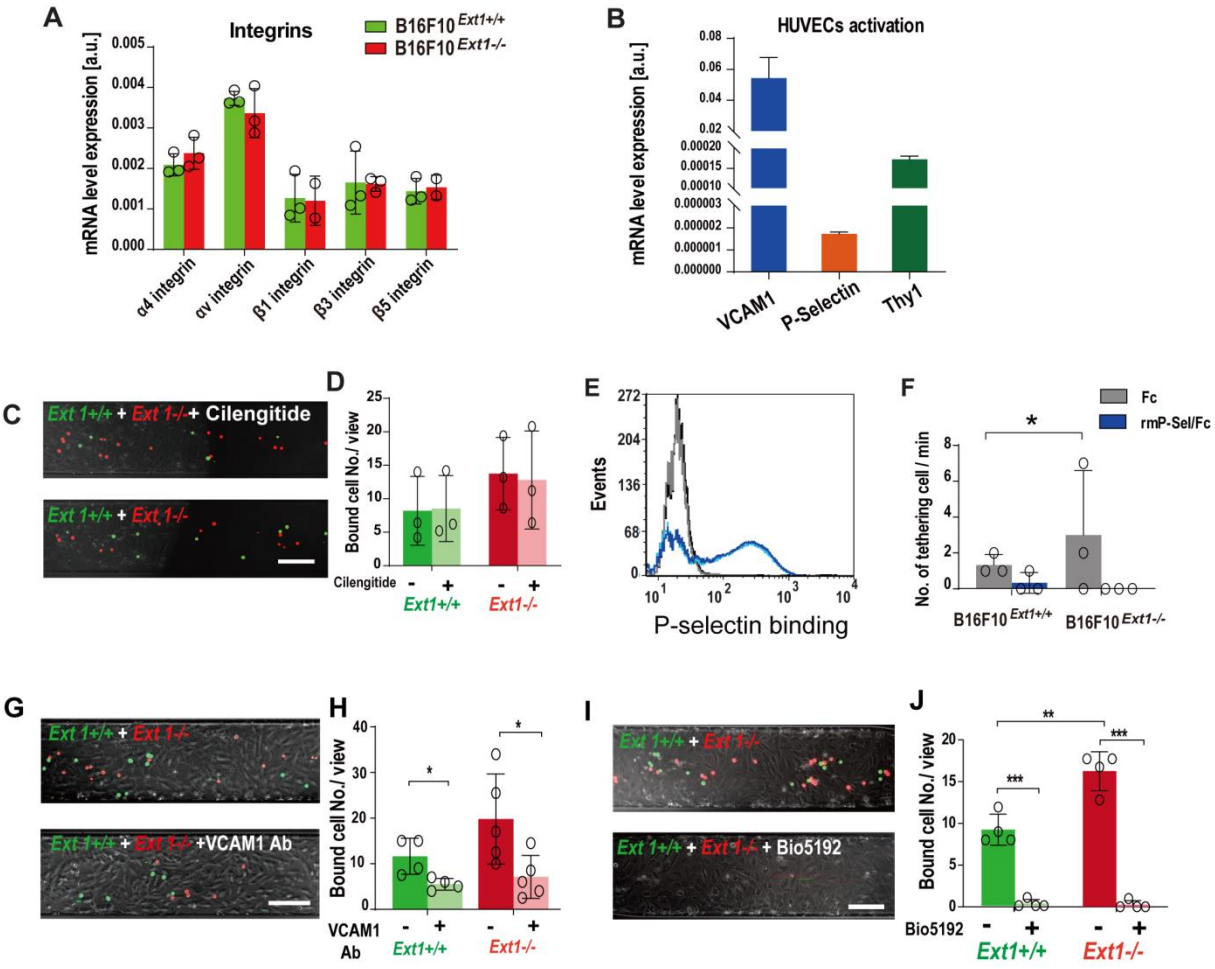

Figure 22. Impact of the endothelial adhesion molecules on melanoma cell adhesion.

(A) Transcription level of Integrins in B16F10$^{Ext1+/+}$ and B16F10$^{Ext1-/-}$ cells measured by qPCR (n = 3). (B) The expression of adhesion molecules on activated HUVECs. (C) The attachment of B16F10 *Ext1+/+* (green) and *Ext1-/-* (red) cells to endothelium in the presence of cilengitide. Blocking Thy1/$\alpha_v\beta_3$ integrin interaction by cilengitide had no impact on B16F10 cells adhesion. (D) Quantification of cell adhesion (n = 3). (E) The binding of B16F10 cells with P-selection in static condition measured by flow cytometry. (F) The adhesion of B16F10 cells to P-selection under dynamic condition. (n = 3). Data were produced by Prof.Dr. Tobias Lange and Sarah Starzonek. Both static and dynamic P-selectin binding assay suggested the contribution of P-selectin is negligible. (G) VCAM1 neutralizing antibodies prevented the vascular adhesion of both B16F10 *Ext1+/+* (green) and *Ext1-/-* (red) cells. (H) Quantification of cell adhesion (n = 4). (I) Blocking VLA4 with Bio5192 abolished B16F10 cell adhesion. (J)

Quantification of cell adhesion (n = 4). Scale bars = 20 µm. Fluorescence and phase contrast images were taken with a Zeiss Observer.Z1 operated by Zen software and equipped with an Axiocam MRm camera. The applied 10x air objective had a numerical aperture of 0.3. Data are presented as the mean ± SD, *P< 0.05. Adapted from **Wang, Y.** *et al.*, 2022[17].

3.19 VLA was not a binding partner of vWF.

To analyze whether vWF can competitively prevent the interaction of VCAM1 to VLA4, the binding affinity between VLA and vWF was measured by SAW-driven biosensors. A dilution series vWF between 0.85 nM and 137 nM in running buffer was injected to measure the binding of vWF to His-tagged VLA4. Figure 23 shows that the binding affinity of vWF to VLA was very low suggesting that a competitive binding of vWF to VLA4 can be excluded.

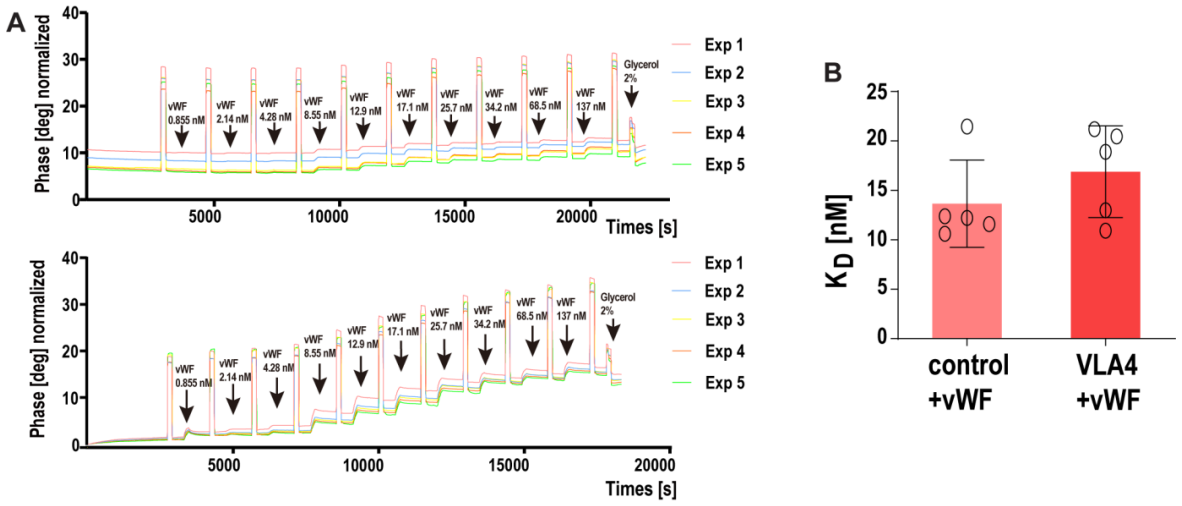

Figure 23. SAW biosensor measure the interaction between VLA4 and vWF.

(A) Phase shift upon addition of vWF to the SAW sensor in the course of time (n = 5). (B) Determination of the dissociation constant (K_D) (n = 5). Data are presented as the mean ± SD, *P< 0.05, **P< 0.005, ***P< 0.0005. Data were produced by Prof.Dr. Gerd Bendas and Martin Heyes. Adapted from **Wang, Y.** *et al.*, 2022[17].

3.20 Complex of HS and vWF promoted repulsion

To mimic the approach of melanoma cells to the endothelium and to measure the acting molecular forces, single molecule force spectroscopy (SMFS) was applied. After coating with PEG, glass slides or AFM tips was covalently linked with recombinant VCAM1 and VLA4 respectively. Where indicated, a preformed complex of vWF and HS was attached to the VLA4 functionalized AFM tip via a covalently linked vWF antibody. The functionalized tip was approached to the surface and the force required to contact the surface was recorded. In comparison to the only VLA4 functionalized tip, a strong repulsive force at the VCAM1-coated glass surface after vWF-HS functionalization was measured. This strong repulsion was indicated by the shift of the force curve towards higher distances (Figure 24A). Then, the onset of repulsion by fitting the force-distance curve using the Hertz model (Figure 24A, dashed lines) was determined. Figure 24B shows the onset of repulsion of VLA4 functionalized tips and tips bearing VLA4 together with the HS-vWF complex. Presence of vWF and HS at the tip surface shifted the repulsion onset from 5 ± 3.6 nm (without vWF-HS) to 51 ± 13.4 nm (with vWF-HS). For comparison, dimeric vWF has an approximate diameter of 60 nm[132], which is in good agreement with the measured onset of repulsion.

To further investigate the molecular connection between VCAM1, VLA4, vWF and HS, the rupture force required to dissociate the bond between VCAM1 and VLA4 was measured. Rupture forces were recorded at different loading rates (Figure 24C, blue circles). In line with Zhang *et al.*[133], two energy barriers that govern the interaction between VCAM1 and VLA4 were identified as indicated by the two linear regression lines in Figure 24C. The bond lifetime (τ) and the bond length (x) for both energy barriers were determined using Bell's model[134]. For the first energy barrier I found that, τ_1 = 0.066 ± 0.006 s and x_1 = 0.70 ± 0.03 Å. The second barrier was characterized by τ_2 = 2.8 ± 0.32 s and x_2 = 3.0 ± 0.06 Å. In control experiments with a VCAM1 neutralizing antibody, the VCAM1-VLA4 interaction was blocked suggesting that the specific interactions were measured (Figure 24D, E). Interestingly, after coupling the vWF-HS complex to the VLA4-functionalized tip (Figure 24C, red circles), the close proximity of the vWF-HS complex had only a very limited impact on the VCAM1-VLA4 interaction (τ_1 = 0.053 ± 0.006 s and x_1 = 0.51 ± 0.03 Å; τ_2 = 3.3 ± 0.79 s and x_2 = 3.0 ± 0.10 Å).

This data suggest that vWF in complex with HS can neither directly interfere with VCAM1 nor VLA4, which is also in line with the biosensor experiments.

Taken together, the biosensor and SMFS measurements suggest that vWF cannot directly interfere with the VLA-VCAM1 interaction. However, strong repulsive forces during the approach of the melanoma cell towards the endothelium may explain the reduced adhesion rate of vWF-wrapped melanoma cells in the microfluidic experiments and consequently also the reduced number of metastatic foci in wild type mice.

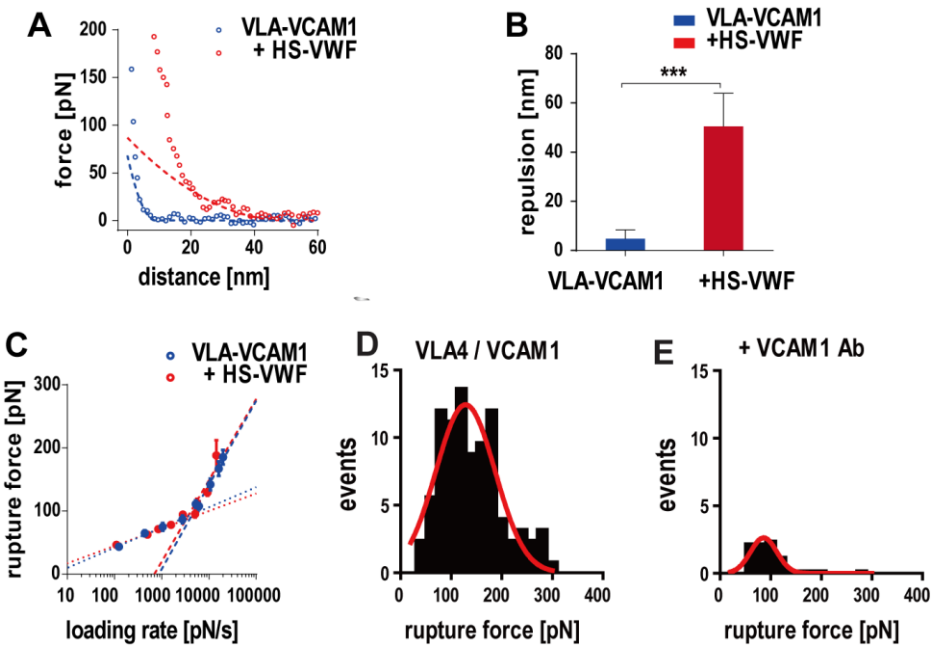

Figure 24. Complex of HS and vWF promoted vascular repulsion

(A) Force-distance curves recorded during the approach of the AFM tip to glass surface. Dashed lines show the curve fitting according to the Hertz model. (B) Quantification of the onset of repulsion. Presence of vWF – HS complex at the AFM tip increased the repulsion force. (C) Rupture force required to dissociate VCAM1 and VLA4 interaction. The coupling of vWF-HS complex had only a very limited impact on the VCAM1-VLA4 interaction (D) Rupture force probability histogram of the VLA4-VCAM1 interaction. (E) Rupture force probability histogram of the VLA4-VCAM1 interaction in the presence of a VCAM1 neutralizing antibody.

Red line corresponds to a Gaussian fit. Data are presented as the mean ± SD, *P< 0.05, **P< 0.005, ***P< 0.0005. Adapted from **Wang, Y.** *et al.*, 2022[17].

4 Discussion

HS have been shown to play important roles in cell migration and metastasis. However, only few studies have focused on the communication between plasmatic proteins and HS, which is expressed on the surface of CTCs. Although, HS has been proposed as an interaction partner of various plasma proteins comprising cytokines, complement factors or members of the coagulation system[135], the contribution and underlying molecular mechanisms of HS in malignant melanoma remains unexplored. These lead us to investigate the impact of tumor cell surface HS, in particular its interaction with plasmatic protein, on the malignant behavior of this specific life-threatening tumor type.

In the present work, the impact of plasmatic vWF on melanoma metastasis was investigated. Melanoma cells with a pronounced HS expression and thus with a large vWF binding ability present a reduced potential to form metastasis. This indicates that plasmatic vWF is antimetastatic and thus potentially able to combat blood circulating cancer cells. Melanoma cells with a reduced HS expression evade recognition by vWF and were prone to form metastasis as their adhesion to the vascular endothelium was increased. In good agreement with this, it was previously published that melanoma cells with an elevated amount of HS at their surface due to the knockdown of HPSE formed less metastatic foci[14].

4.1 The characterization of HS

Altered expression and structural variability of HSPGs have been associated with an extensive remodeling of tumor microenvironment where HSPGs not only contribute to the formation of a structural framework for tumor growth but are also involved in the regulation of cell-matrix and cell-cell interactions, and cell signaling[136] . They are able to modulate cancer cell phenotype, to be involved in the development of drug resistance, and to induce neoangiogenesis[137]. Differential expression and structure/activity modifications of HSPGs have been found in several cancers and may correlate with either inhibitory or tumor-promoting activity[138].

As such, extensive work has been devoted to studying HS structure and function[18, 139]. In the present work, cancer cell-exposed glycosaminoglycans were analyzed by a series of different methods: flow cytometry, fluorescence, gel chromatography, NP titration assay and super-resolution microscopy.With gel chromatography, it was possible to estimate the molecular weight and relative amounts of HS and CS chains (Figure 11A - F). The molecular weight of HS chains expressed on MV3 shCTL cells (between 43kDa and 210kDa) were larger than the HS chains exposed by MV3 shEXT1 cells (between 30kDa and 43kDa) (Figure 11B). In contrast to the changed molecular weight, the relative amount of HS chains was similar in MV3 shEXT1 and MV3 shCTL cells. Next to the humane melanoma cells, also the CRIPSR/Cas9 engineered cells were characterizes by gel chromatography. The molecular weight of HS on B16F10$^{EXT1+/+}$ cells was about 43kDa. The B16F10$^{EXT1-/-}$ cells expressed no HS (Figure 11E).

Nanoscaled morphologies of HSPG was shown on STED microscopy images (Figure 12A-D), which also confirmed that knockdown EXT1 expression changed the length of HS chains but not HSPG density. To validate the data obtained by gel chromatography, a previously published method basing on NP titration was used[20]. The corresponding results confirmed that the glycocalyx of melanoma cells is largely composed of HS chains with a length of 100 to 200 nm producing a glycocalyx layer with a thickness of approximately 20 nm (Figure 13). A scaled schematic drawing of the glycan analysis is shown in Figure 25A, B and C

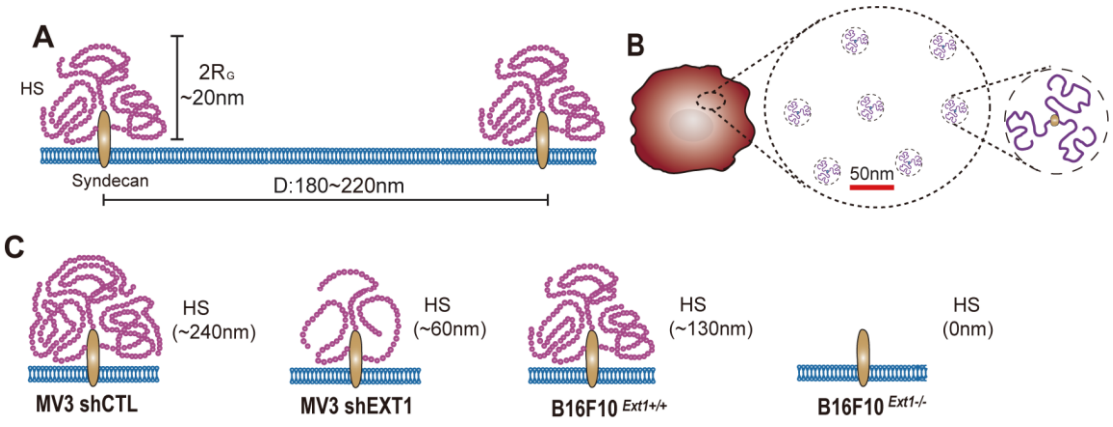

Figure 25. Side view and top view of cell surface exposed HS proteoglycan.

(A) Side view of membrane bound HS proteoglycan. The thickness of the HS layer is twice the radius of gyration (R_G). (B) Top view of cell surface HS proteoglycan distribution. Scale bars = 50 nm. (C) Schematic painting of the different lengths of HS proteoglycans expressed on genetically engineered MV3 and B16F10 cells. Adapted from **Wang, Y.** *et al.*, 2022[17].

4.2 Complex formed between vWF and tumor cell surface HS

By using different vWF mutations and inhibitors, HS was identified as main binding partner of vWF (Figure 7, 8). Experiments with mutated vWF also indicated that the interaction between vWF and HS at the melanoma cell surface required the presence of the A1 domain. In its globular conformation vWF hide the A1 domain, whereas stretching of vWF e.g. through shear forces promote the exposure of the A1 domain. This suggests that during the interaction with the melanoma cell surface, vWF is at least partially elongated and that the exposed A1 domains are almost all occupied by tumor cell surface HS (Figure 26). That long HS chains were assumed to interact with multiple A1 domains leading to a tight molecular complex between HS and vWF comparable to a tape of hook and loop fastener. This complex formation is accompanied with a stretching of the HS chain.

To obtain experimental evidence for the assumption, I was aimed to determine whether cell surface bound vWF expose unoccupied A1 domains. Therefore, the vWF encapsulated melanoma cells were probed with washed platelets. Platelets express the A1 domain ligand glycoprotein Ib-α and binding of platelets to the melanoma cells indicates the availability of free A1 domains. As shown in Figure 26 A, B, overall rate of platelet binding was low and the presence of vWF at the cell surface had no impact on the binding rate suggesting that most A1 domains are either not accessible or already occupied by HS.

However and in contrast to all other plasma proteins, vWF is a very large multimer in the gigadalton range. Even after ADAMTS13 degradation, blood circulating vWF multimers are composed of about 200 monomers[140]. Because each monomer bearing a binding site for HS, vWF multimers have an enormous potential to form a tight complex cell surface HS. In line with the supposed tight complex formed between HS and vWF, cell surface bound multimeric vWF was inaccessible for platelets (Figure 26). This suggests the lack of free A1

domain on cell bound vWF, but also an irreversible character of the HS-vWF complex. Initial experiments, in which MV3 cells was spiked with whole human blood showed that vWF mainly accumulated on the surface of melanoma cells but not leukocytes (Figure 5A, B). This specificity highlights the selective character of vWF to recognize unwanted cells within the circulation. The origin of this specificity remained to be elusive as also leucocytes express HS on their surface[141]. However, the expression and sulfation pattern of the leucocyte-exposed HS might be different and less potent to interact with vWF[142 143].

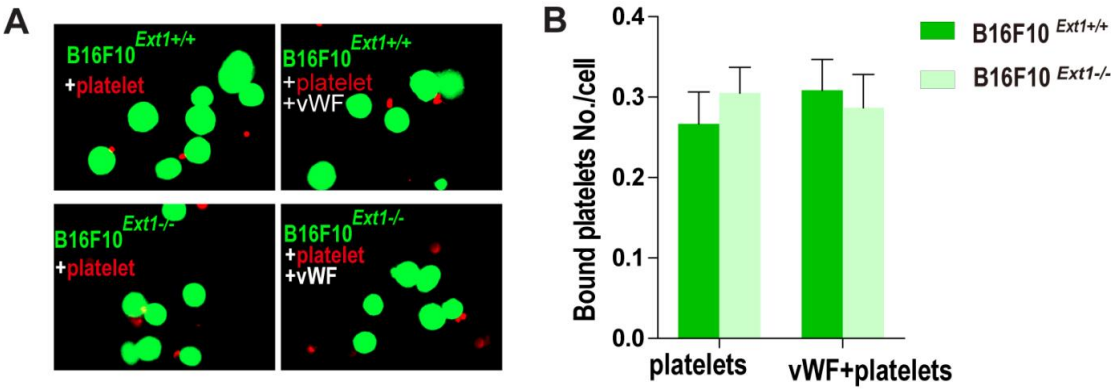

Figure 26. Platelets binding to B16F10 cells in the presence or absence of vWF.

(A) Binding of platelets to B16F10 tumor cells with or without the presence of vWF. (B) Quantification of platelets binding (n = 50). Platelets binding to tumor cells was not affected by vWF. Adapted from **Wang, Y.** *et al.*, 2022[17].

4.3 The triangular interaction between HS, integrins and plasmatic vWF

In the present study, the contribute of integrins to the binding of soluble vWF to flowing melanoma cells was confirmed (Figure 7). However, in comparison to HS, their impact was less relevant (Figure 15). Moreover, the binding activity of integrins was even largely dependent on HS. The molecular interplay between the glycocalyx of cancer cells and integrins has previously been reported. The HS exposing proteoglycan SDC-4 or SCD-1 were shown to directly promote αvβ3 or β5 integrin activation[144, 145]. Others postulated that

especially long glycan chains can activate integrins through an energetic trap formation[128]. It is important to note that most of the previous research investigated the cross talk between the glycocalyx and integrins in the context of cell adhesion under static conditions. The triangular communication between integrins, HS and vWF was studied in suspension and dynamic flow conditions. Therefore, previous postulated mechanisms need to be reevaluated and eventually adjusted.

In conclusion, HS together with integrins orchestrate the binding of soluble vWF. These findings was illustrated in a schematic drawing (Figure 27). To which extend other plasma proteins are recognized by HS in concert with integrins remained to be clarified.

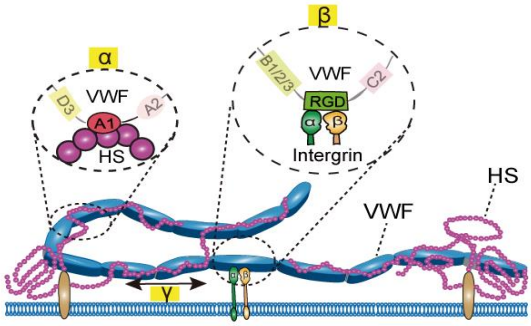

Figure 27. Schematic drawing of the interaction between HS, integrins, and vWF.

The HS-related impact on vWF binding was defined as α. The HS-independent integrin activity was defined as β. The HS-dependent integrin activity defines as γ. All α, β, and γ contribute to vWF binding. Among them, α plays the main role in vWF binding. Adapted from **Wang, Y.** *et al.*, 2022[17].

4.4 The formation of vWF-HS complex promoted repulsion and thus prevented vascular adhesion

The interaction between circulating melanoma cells and the vascular endothelium is complex and different adhesion molecules have been identified. In the experimental setup,

B16F10 cells adhere to the endothelium through the VLA4/VCAM1 axis, whereas the previously reported interaction between Thy-1 and αvβ3 integrin[131] appeared to be less relevant in the experiment (Figure 22C, D). Additionally, both under static and dynamic conditions, B16F10 cells present only a minor ability to interact with P-selectin (Figure 22E, F). Interestingly, by SAW biosensor measurements, vWF was proved can't interfere directly with the VLA4/VCAM1 interaction (Figure 23).

In microfluidic experiments, presence of vWF attenuated significantly the vascular adhesion of both murine and human tumor cells with longer HS chain length but not tumor cells with shorter or completely lacking HS (Figure 20 A - D). SMFS was used to measure the molecular forces between tumor cells and endothelium (Figure 24 A). The formation of HS-vWF complex performed strong repulsion, and thus reduced the possibility of tumor cell surface VLA4 interacting with VCAM1 on endothelium (Figure 24 B, C). But the rupture force required to dissociate VCAM1 and VLA4 was not affected (Figure 24 D, E), indicating that VWF in complex with HS can neither directly interfere with VCAM1 nor VLA4.

Interestingly, it was also observed in the absence of vWF, B16F10$^{Ext1-/-}$ cells bound more frequent to the endothelial cell layer than the B16F10$^{Ext1+/+}$ cells (Figure 20 A, B). By ECIS, RICM and STED-NP titration measurements (Figure 21), it can be explained the HS related effect was due to tumor cells lacking HS expression can approach closer to the adhesive surface.

The schematic overview in Figure 28 shows the interference of vWF with the binding of melanoma cells to the vascular wall. Blood CTCs exposing higher HS at their surface were encapsulated by plasmatic vWF, which formed a tight molecular complex with HS at the surface of tumor cells. The vWF-HS complex promoted the repulsion of the tumor cell from the endothelium, and thus prevented vascular adhesion and attenuated hematogenous metastasis. Whereas, tumor cell with reduced length of HS chains or complete lack of HS was associated with significantly reduced vWF binding, and thus easy to adhesion on vessel wall and increased metastasis.

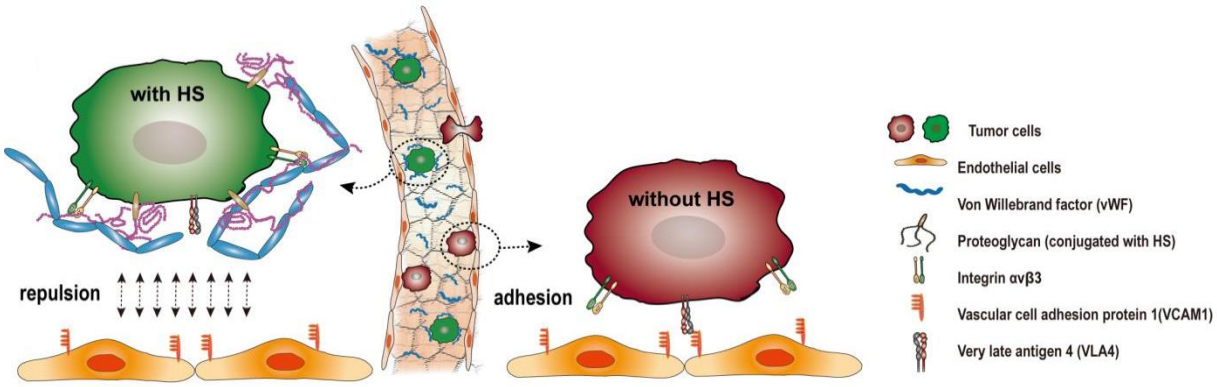

Figure 28. Schematic model of current study.

Blood CTCs with higher HS expressed on surface could interact with plasmatic vWF, and form a tight vWF-HS complex which promoted vascular repulsion and thus prevented adhesion and further hematogenous metastasis. However, tumor cells without HS expression could not bind with vWF and thus easy to adhesion on endothelium and promote metastasis formation. Adapted from **Wang, Y.** *et al.*, 2022[17].

4.5 The dual function of vWF in tumor metastasis

In vivo experiments showed in wt mice, that B16F10$^{Ext1-/-}$ formed significantly more metastatic foci than the control cells (B16F10$^{Ext1+/+}$), while in vWF knockout mice, the discrepancy of metastasis disappeared, B16F10$^{Ext1+/+}$ cells formed as much metastasis as B16F10$^{Ext1-/-}$ cells (Figure 16A - C). These data implied in wt mice, tumor cells with longer HS chains will be recognized and encapsulated by plasmatic vWF, the HS-vWF formed tight complex on cell surface increased repulsion and reduced adhesion ability to endothelium, and thus form reduced metastasis. In agree with previous research, these results suggesting the antimetastatic role of vWF. Additionally, HS was barely detectable in metastases formed by B16F10$^{Ext1-/-}$ cells when compared to foci of control cells (Figure 16D, E) further confirmed that tumor cells lacking HS at cell surface were easy to escape the recognition of plasmatic vWF and thus easy to form metastasis.

Next to the animal data, tissue samples from melanoma patients also showing that melanoma cells within the primary melanoma tissue express higher HS levels than melanoma cells of metastatic foci (Figure 17). In agree with patient tissue staining, decreased HS-related genes expression was found in melanoma metastases (Figure 18A). And the low expression level of HS-related genes also related to a reduced patients' survival (Figure 18B). Taken together, the analysis of melanoma patients' data verified that melanoma cells with less HS expression could escape the recognition of vWF and form metastasis.

In contrast to the evidence supporting a anti-metastatic role for plasmatic vWF, ULvWF fiber were postulated to promote metastasis by anchoring blood CTCs at their site of metastasis[59, 75]. Though the mechanistic data are missing, this points towards a dual function of vWF. The formation of ULvWF fibers was due to the overwhelming secretion of vWF by tumoral endothelial cells in combination with a lack of active ADAMTS13 which can promote extensive vWF stretching. But in a balanced physiological situation in which ULvWF fibers are barely formed, plasmatic vWF may prevent metastasis. In a more unbalanced homeostatic situation, present e.g. in late staged melanoma patients with distant metastasis, ULvWF fibers might form[146]. Whether ULvWF fibers can directly contribute to metastasis formation is unclear and further research is required to identify molecular interaction partners showing the specific contribution of ULvWF fibers for metastasis development.

4.6 Conclusion

In summary, I found that HS-mediated recognition of cancer cells by plasmatic vWF can reduce metastasis. Accordingly, one could assume that the application of vWF to tumor patients e.g., during events promoting the release of CTCs into the circulation such as radiation, tissue biopsies and surgery[147, 148] may prevent hematogenous metastasis. However, because the exclusive administration of vWF may increase the risk of ULvWF formation, co-application of ADAMTS13 appeared to be more advisable. Also the therapeutic manipulation of the HS, exposed by CTCs, through cell surface adhesive glycan mimetics might present anti-metastatic effects. The current study focused on melanoma

metastasis; however additional data on breast cancer CTCs indicate that a more general anti-metastatic mechanism has been discovered. [17]

Publication

This thesis has been published in:

Wang, Y. *et al.* Heparan sulfate dependent binding of plasmatic von Willebrand factor to blood circulating melanoma cells attenuates metastasis. *Matrix Biol* **111**, 76-94 (2022).

References

1. Weinbaum, S., Tarbell, J.M. & Damiano, E.R. The structure and function of the endothelial glycocalyx layer. *Annu Rev Biomed Eng* **9**, 121-167 (2007).

2. Shriver, Z., Capila, I., Venkataraman, G. & Sasisekharan, R. Heparin and heparan sulfate: analyzing structure and microheterogeneity. *Handb Exp Pharmacol*, 159-176 (2012).

3. Purushothaman, A., Sugahara, K. & Faissner, A. Chondroitin sulfate "wobble motifs" modulate maintenance and differentiation of neural stem cells and their progeny. *J Biol Chem* **287**, 2935-2942 (2012).

4. Yamada, S. & Sugahara, K. Potential therapeutic application of chondroitin sulfate/dermatan sulfate. *Curr Drug Discov Technol* **5**, 289-301 (2008).

5. Pomin, V.H. Keratan sulfate: an up-to-date review. *Int J Biol Macromol* **72**, 282-289 (2015).

6. Li, L., Ly, M. & Linhardt, R.J. Proteoglycan sequence. *Mol Biosyst* **8**, 1613-1625 (2012).

7. Becker, B.F., Jacob, M., Leipert, S., Salmon, A.H.J. & Chappell, D. Degradation of the endothelial glycocalyx in clinical settings: searching for the sheddases. *Br J Clin Pharmacol* **80**, 389-402 (2015).

8. Broekhuizen, L.N. *et al.* Endothelial glycocalyx as potential diagnostic and therapeutic target in cardiovascular disease. *Curr Opin Lipidol* **20**, 57-62 (2009).

9. Arnold, K.M. *et al.* Modernization of Enoxaparin Molecular Weight Determination Using Homogeneous Standards. *Pharmaceuticals (Basel)* **10**, 66 (2017).

10. Sarrazin, S., Lamanna, W.C. & Esko, J.D. Heparan sulfate proteoglycans. *Cold Spring Harb Perspect Biol* **3**, a004952 (2011).

11. Fu, B.M. & Tarbell, J.M. Mechano-sensing and transduction by endothelial surface glycocalyx: composition, structure, and function. *Wiley Interdiscip Rev Syst Biol Med* **5**, 381-390 (2013).

12. Kang, H. *et al.* Cancer Cell Glycocalyx and Its Significance in Cancer Progression. *Int J Mol Sci* **19**, 2484 (2018).

13. Tarbell, J.M. & Cancel, L.M. The glycocalyx and its significance in human medicine. *J Intern Med* **280**, 97-113 (2016).

14. Yang, Y. *et al.* Nuclear heparanase-1 activity suppresses melanoma progression via its DNA-binding affinity. *Oncogene* **34**, 5832-5842 (2015).

15. Cherfils-Vicini, J. *et al.* Cancer cells induce immune escape via glycocalyx changes controlled by the telomeric protein TRF2. *EMBO J* **38** (2019).

16. Beauvais, D.M. & Rapraeger, A.C. Syndecan-1-mediated cell spreading requires signaling by alphavbeta3 integrins in human breast carcinoma cells. *Exp Cell Res* **286**, 219-232 (2003).

17. Wang, Y. *et al.* Heparan sulfate dependent binding of plasmatic von Willebrand factor to blood circulating melanoma cells attenuates metastasis. *Matrix Biol* **111**, 76-94 (2022).

18. Li, J.P. & Kusche-Gullberg, M. Heparan Sulfate: Biosynthesis, Structure, and Function. *Int Rev Cell Mol Biol* **325**, 215-273 (2016).

19. Clerc, O. *et al.* A pipeline to translate glycosaminoglycan sequences into 3D models. Application to the exploration of glycosaminoglycan conformational space. *Glycobiology* **29**, 36-44 (2019).

20. von Palubitzki, L. *et al.* Differences of the tumour cell glycocalyx affect binding of capsaicin-loaded chitosan nanocapsules. *Sci Rep* **10**, 22443 (2020).

21. Esko, J.D., Kimata, K. & Lindahl, U. Proteoglycans and Sulfated Glycosaminoglycans, in *Essentials of Glycobiology*. (eds. A. Varki *et al.*) (Cold Spring Harbor Laboratory Press Copyright © 2009, The Consortium of Glycobiology Editors, La Jolla, California., Cold Spring Harbor (NY); 2009).

22. Couchman, J.R., Multhaupt, H. & Sanderson, R.D. Recent Insights into Cell Surface Heparan Sulphate Proteoglycans and Cancer. *F1000Res* **5** (2016).

23. Ghossoub, R. *et al.* Tetraspanin-6 negatively regulates exosome production. *Proc Natl Acad Sci U S A* **117**, 5913-5922 (2020).

24. Bishop, J.R., Schuksz, M. & Esko, J.D. Heparan sulphate proteoglycans fine-tune mammalian physiology. *Nature* **446**, 1030-1037 (2007).

25. Sarrazin, S., Lamanna, W.C. & Esko, J.D. Heparan sulfate proteoglycans. *Cold Spring Harb Perspect Biol* **3** (2011).

26. Bishop, J.R., Schuksz, M. & Esko, J.D. Heparan sulphate proteoglycans fine-tune mammalian physiology. *Nature* **446**, 1030-1037 (2007).

27. Faria-Ramos, I. *et al.* Heparan Sulfate Glycosaminoglycans: (Un)Expected Allies in Cancer Clinical Management. *Biomolecules* **11**, 136 (2021).

28. Vallet, S.D., Clerc, O. & Ricard-Blum, S. Glycosaminoglycan-Protein Interactions: The First Draft of the Glycosaminoglycan Interactome. *J Histochem Cytochem* **69**, 93-104 (2021).

29. Fabregat, A. *et al.* Reactome pathway analysis: a high-performance in-memory approach. *BMC Bioinformatics* **18**, 142 (2017).

30. Jassal, B. *et al.* The reactome pathway knowledgebase. *Nucleic Acids Res* **48**, D498-d503 (2020).

31. Capila, I. & Linhardt, R.J. Heparin-protein interactions. *Angew Chem Int Ed Engl* **41**, 391-412 (2002).

32. Kjellén, L. & Lindahl, U. Specificity of glycosaminoglycan-protein interactions. *Curr Opin Struct Biol* **50**, 101-108 (2018).

33. Manning, G.S. Limiting laws and counterion condensation in polyelectrolyte solutions: V. Further development of the chemical model. *Biophysical Chemistry* **9**, 65-70 (1978).

34. Knelson, E.H., Nee, J.C. & Blobe, G.C. Heparan sulfate signaling in cancer. *Trends Biochem Sci* **39**, 277-288 (2014).

35. Hassan, N., Greve, B., Espinoza-Sánchez, N.A. & Götte, M. Cell-surface heparan sulfate proteoglycans as multifunctional integrators of signaling in cancer. *Cell Signal* **77**, 109822 (2021).

36. Raman, K. & Kuberan, B. Chemical Tumor Biology of Heparan Sulfate Proteoglycans. *Curr Chem Biol* **4**, 20-31 (2010).

37. Peterson, S.M. *et al.* Human Sulfatase 2 inhibits in vivo tumor growth of MDA-MB-231 human breast cancer xenografts. *BMC Cancer* **10**, 427 (2010).

38. Mikami, S. *et al.* Loss of syndecan-1 and increased expression of heparanase in invasive esophageal carcinomas. *Jpn J Cancer Res* **92**, 1062-1073 (2001).

39. Kawahara, R. *et al.* Agrin and perlecan mediate tumorigenic processes in oral squamous cell carcinoma. *PLoS One* **9**, e115004 (2014).

40. Vreys, V. & David, G. Mammalian heparanase: what is the message? *J Cell Mol Med* **11**, 427-452 (2007).

41. Ding, Q. *et al.* CXCL9: evidence and contradictions for its role in tumor progression. *Cancer Med* **5**, 3246-3259 (2016).

42. Harlin, H. *et al.* Chemokine expression in melanoma metastases associated with CD8+ T-cell recruitment. *Cancer Res* **69**, 3077-3085 (2009).

43. Koliopanos, A. *et al.* Heparanase expression in primary and metastatic pancreatic cancer. *Cancer Res* **61**, 4655-4659 (2001).

44. John, A. *et al.* Urothelial Carcinoma of the Bladder Induces Endothelial Cell Activation and Hypercoagulation. *Mol Cancer Res* **18**, 1099-1109 (2020).

45. Schadendorf, D. *et al.* Melanoma. *Lancet* **392**, 971-984 (2018).

46. Chen, L., Bode, A.M. & Dong, Z. Circulating Tumor Cells: Moving Biological Insights into Detection. *Theranostics* **7**, 2606-2619 (2017).

47. Ward, M.P. *et al.* Platelets, immune cells and the coagulation cascade; friend or foe of the circulating tumour cell? *Mol Cancer* **20**, 59 (2021).

48. Leblanc, R. & Peyruchaud, O. Metastasis: new functional implications of platelets and megakaryocytes. *Blood* **128**, 24-31 (2016).

49. Labelle, M., Begum, S. & Hynes, R.O. Direct signaling between platelets and cancer cells induces an epithelial-mesenchymal-like transition and promotes metastasis. *Cancer Cell* **20**, 576-590 (2011).

50. Chivukula, V.K., Krog, B.L., Nauseef, J.T., Henry, M.D. & Vigmostad, S.C. Alterations in cancer cell mechanical properties after fluid shear stress exposure: a micropipette aspiration study. *Cell Health Cytoskelet* **7**, 25-35 (2015).

51. Pardoll, D.M. The blockade of immune checkpoints in cancer immunotherapy. *Nat Rev Cancer* **12**, 252-264 (2012).

52. Wang, Y. *et al.* PD-L1 Expression in Circulating Tumor Cells Increases during Radio(chemo)therapy and Indicates Poor Prognosis in Non-small Cell Lung Cancer. *Sci Rep* **9**, 566 (2019).

53. Baccelli, I. *et al.* Identification of a population of blood circulating tumor cells from breast cancer patients that initiates metastasis in a xenograft assay. *Nat Biotechnol* **31**, 539-544 (2013).

54. Cabel, L. *et al.* Circulating tumor cells: clinical validity and utility. *International journal of clinical oncology* **22**, 421-430 (2017).

55. Schlesinger, M. *et al.* The role of VLA-4 binding for experimental melanoma metastasis and its inhibition by heparin. *Thrombosis research* **133**, 855-862 (2014).

56. Schlesinger, M. *et al.* The inhibition of the integrin VLA-4 in MV3 melanoma cell binding by non-anticoagulant heparin derivatives. *Thrombosis research* **129**, 603-610 (2012).

57. Saalbach, A. *et al.* Interaction of human Thy-1 (CD 90) with the integrin alphavbeta3 (CD51/CD61): an important mechanism mediating melanoma cell adhesion to activated endothelium. *Oncogene* **24**, 4710-4720 (2005).

58. Reymond, N., d'Água, B.B. & Ridley, A.J. Crossing the endothelial barrier during metastasis. *Nature Reviews Cancer* **13**, 858-870 (2013).

59. Bauer, A.T. *et al.* von Willebrand factor fibers promote cancer-associated platelet aggregation in malignant melanoma of mice and humans. *Blood* **125**, 3153-3163 (2015).

60. Mojzisch, A. & Brehm, M.A. The Manifold Cellular Functions of von Willebrand Factor. *Cells* **10** (2021).

61. Ruggeri, Z.M. The role of von Willebrand factor in thrombus formation. *Thrombosis research* **120 Suppl 1**, S5-9 (2007).

62. Haberichter, S.L., Fahs, S.A. & Montgomery, R.R. von Willebrand factor storage and multimerization: 2 independent intracellular processes. *Blood* **96**, 1808-1815 (2000).

63. Wagner, D.D. Cell biology of von Willebrand factor. *Annual review of cell biology* **6**, 217-246 (1990).

64. Li, F., Li, C.Q., Moake, J.L., López, J.A. & McIntire, L.V. Shear stress-induced binding of large and unusually large von Willebrand factor to human platelet glycoprotein Ibalpha. *Annals of biomedical engineering* **32**, 961-969 (2004).

65. Alexander-Katz, A., Schneider, M.F., Schneider, S.W., Wixforth, A. & Netz, R.R. Shear-flow-induced unfolding of polymeric globules. *Physical review letters* **97**, 138101 (2006).

66. Schneider, S.W. *et al.* Shear-induced unfolding triggers adhesion of von Willebrand factor fibers. *Proceedings of the National Academy of Sciences of the United States of America* **104**, 7899-7903 (2007).

67. Singh, I., Themistou, E., Porcar, L. & Neelamegham, S. Fluid shear induces conformation change in human blood protein von Willebrand factor in solution. *Biophysical journal* **96**, 2313-2320 (2009).

68. Wijeratne, S.S. *et al.* Mechanical activation of a multimeric adhesive protein through domain conformational change. *Physical review letters* **110**, 108102 (2013).

69. Zheng, X. *et al.* Structure of von Willebrand factor-cleaving protease (ADAMTS13), a metalloprotease involved in thrombotic thrombocytopenic purpura. *The Journal of biological chemistry* **276**, 41059-41063 (2001).

70. Casari, C. *et al.* Accelerated uptake of VWF/platelet complexes in macrophages contributes to VWD type 2B-associated thrombocytopenia. *Blood* **122**, 2893-2902 (2013).

71. Kawecki, C., Lenting, P.J. & Denis, C.V. von Willebrand factor and inflammation. *J Thromb Haemost* **15**, 1285-1294 (2017).

72. Starke, R.D. *et al.* Endothelial von Willebrand factor regulates angiogenesis. *Blood* **117**, 1071-1080 (2011).

73. Franchini, M., Frattini, F., Crestani, S., Bonfanti, C. & Lippi, G. von Willebrand factor and cancer: a renewed interest. *Thrombosis research* **131**, 290-292 (2013).

74. Dhami, S.P.S. *et al.* Breast cancer cells mediate endothelial cell activation, promoting von Willebrand factor release, tumor adhesion, and transendothelial migration. *J Thromb Haemost* (2022).

75. Feinauer, M.J. *et al.* Local blood coagulation drives cancer cell arrest and brain metastasis in a mouse model. *Blood* **137**, 1219-1232 (2021).

76. Goertz, L. *et al.* Heparins that block VEGF-A-mediated von Willebrand factor fiber generation are potent inhibitors of hematogenous but not lymphatic metastasis. *Oncotarget* **7**, 68527-68545 (2016).

77. Hatzipantelis, E.S. *et al.* Thrombomodulin and von Willebrand factor: relation to endothelial dysfunction and disease outcome in children with acute lymphoblastic leukemia. *Acta Haematol* **125**, 130-135 (2011).

78. Schellerer, V.S. *et al.* The clinical value of von Willebrand factor in colorectal carcinomas. *Am J Transl Res* **3**, 445-453 (2011).

79. Wang, W.S. *et al.* Plasma von Willebrand factor level as a prognostic indicator of patients with metastatic colorectal carcinoma. *World J Gastroenterol* **11**, 2166-2170 (2005).

80. Zietek, Z., Iwan-Zietek, I., Paczulski, R., Kotschy, M. & Wolski, Z. von Willebrand factor antigen in blood plasma of patients with urinary bladder carcinoma. *Thromb Res* **83**, 399-402 (1996).

81. Gadducci, A. *et al.* Pretreatment plasma levels of fibrinopeptide-A (FPA), D-dimer (DD), and von Willebrand factor (vWF) in patients with ovarian carcinoma. *Gynecologic oncology* **53**, 352-356 (1994).

82. Terraube, V. *et al.* Increased metastatic potential of tumor cells in von Willebrand factor-deficient mice. *Journal of thrombosis and haemostasis : JTH* **4**, 519-526 (2006).

83. Mochizuki, S. *et al.* Effect of ADAM28 on carcinoma cell metastasis by cleavage of von Willebrand factor. *J Natl Cancer Inst* **104**, 906-922 (2012).

84. Afratis, N. *et al.* Glycosaminoglycans: key players in cancer cell biology and treatment. *Febs j* **279**, 1177-1197 (2012).

85. Faria-Ramos, I. *et al.* Heparan Sulfate Glycosaminoglycans: (Un)Expected Allies in Cancer Clinical Management. *Biomolecules* **11** (2021).

86. Nikitovic, D., Mytilinaiou, M., Berdiaki, A., Karamanos, N.K. & Tzanakakis, G.N. Heparan sulfate proteoglycans and heparin regulate melanoma cell functions. *Biochim Biophys Acta* **1840**, 2471-2481 (2014).

87. Bayarri-Lara, C. *et al.* Circulating Tumor Cells Identify Early Recurrence in Patients with Non-Small Cell Lung Cancer Undergoing Radical Resection. *PLoS One* **11**, e0148659 (2016).

88. Delgado-Ureña, M. *et al.* Circulating tumor cells criteria (CyCAR) versus standard RECIST criteria for treatment response assessment in metastatic colorectal cancer patients. *J Transl Med* **16**, 251 (2018).

89. Mamdouhi, T., Twomey, J.D., McSweeney, K.M. & Zhang, B. Fugitives on the run: circulating tumor cells (CTCs) in metastatic diseases. *Cancer Metastasis Rev* **38**, 297-305 (2019).

90. Tsai, W.-S. *et al.* Circulating Tumor Cell Count Correlates with Colorectal Neoplasm Progression and Is a Prognostic Marker for Distant Metastasis in Non-Metastatic Patients. *Scientific Reports* **6**, 24517 (2016).

91. Al-Mehdi, A.B. *et al.* Intravascular origin of metastasis from the proliferation of endothelium-attached tumor cells: a new model for metastasis. *Nat Med* **6**, 100-102 (2000).

92. Rejniak, K.A. Circulating Tumor Cells: When a Solid Tumor Meets a Fluid Microenvironment. *Adv Exp Med Biol* **936**, 93-106 (2016).

93. Garrido-Navas, C. *et al.* Cooperative and Escaping Mechanisms between Circulating Tumor Cells and Blood Constituents. *Cells* **8** (2019).

94. Young, A. *et al.* Thrombosis and cancer. *Nature Reviews Clinical Oncology* **9**, 437-449 (2012).

95. Sørensen, H.T., Mellemkjaer, L., Olsen, J.H. & Baron, J.A. Prognosis of cancers associated with venous thromboembolism. *The New England journal of medicine* **343**, 1846-1850 (2000).

96. Stark, K. & Massberg, S. Interplay between inflammation and thrombosis in cardiovascular pathology. *Nature Reviews Cardiology* **18**, 666-682 (2021).

97. O'Regan, N. *et al.* A novel role for von Willebrand factor in the pathogenesis of experimental cerebral malaria. *Blood* **127**, 1192-1201 (2016).

98. Perico, L. *et al.* Immunity, endothelial injury and complement-induced coagulopathy in COVID-19. *Nature Reviews Nephrology* **17**, 46-64 (2021).

99. Carlson, P. *et al.* Targeting the perivascular niche sensitizes disseminated tumour cells to chemotherapy. *Nature Cell Biology* **21**, 238-250 (2019).

100. Malehmir, M. *et al.* Platelet GPIbα is a mediator and potential interventional target for NASH and subsequent liver cancer. *Nature Medicine* **25**, 641-655 (2019).

101. Oleksowicz, L., Dutcher, J.P., Deleon-Fernandez, M., Paietta, E. & Etkind, P. Human breast carcinoma cells synthesize a protein immunorelated to platelet glycoprotein-Ib alpha with different functional properties. *The Journal of laboratory and clinical medicine* **129**, 337-346 (1997).

102. Floyd, C.M., Irani, K., Kind, P.D. & Kessler, C.M. von Willebrand factor interacts with malignant hematopoietic cell lines: evidence for the presence of specific binding sites and modification of von Willebrand factor structure and function. *The Journal of laboratory and clinical medicine* **119**, 467-476 (1992).

103. Pilch, J., Habermann, R. & Felding-Habermann, B. Unique ability of integrin alpha(v)beta 3 to support tumor cell arrest under dynamic flow conditions. *The Journal of biological chemistry* **277**, 21930-21938 (2002).

104. Paszek, M.J., Boettiger, D., Weaver, V.M. & Hammer, D.A. Integrin clustering is driven by mechanical resistance from the glycocalyx and the substrate. *PLoS Comput Biol* **5**, e1000604-e1000604 (2009).

105. Paszek, M.J. *et al.* The cancer glycocalyx mechanically primes integrin-mediated growth and survival. *Nature* **511**, 319-325 (2014).

106. Kalagara, T. *et al.* The endothelial glycocalyx anchors von Willebrand factor fibers to the vascular endothelium. *Blood Adv* **2**, 2347-2357 (2018).

107. Watts, C.G. *et al.* Association Between Melanoma Detected During Routine Skin Checks and Mortality. *JAMA Dermatol* **157**, 1425-1436 (2021).

108. Guy, G.P., Jr. *et al.* Vital signs: melanoma incidence and mortality trends and projections - United States, 1982-2030. *MMWR Morb Mortal Wkly Rep* **64**, 591-596 (2015).

109. Tripp, M.K., Watson, M., Balk, S.J., Swetter, S.M. & Gershenwald, J.E. State of the science on prevention and screening to reduce melanoma incidence and mortality: The time is now. *CA Cancer J Clin* **66**, 460-480 (2016).

110. Goerge, T. *et al.* Tumor-derived matrix metalloproteinase-1 targets endothelial proteinase-activated receptor 1 promoting endothelial cell activation. *Cancer Res* **66**, 7766-7774 (2006).

111. Hoadley, K.A. *et al.* Cell-of-Origin Patterns Dominate the Molecular Classification of 10,000 Tumors from 33 Types of Cancer. *Cell* **173**, 291-304.e296 (2018).

112. Cerami, E. *et al.* The cBio Cancer Genomics Portal: An Open Platform for Exploring Multidimensional Cancer Genomics Data. *Cancer discovery* **2**, 401-404 (2012).

113. Gao, J. *et al.* Integrative analysis of complex cancer genomics and clinical profiles using the cBioPortal. *Sci Signal* **6**, pl1 (2013).

114. Schneider, C.A., Rasband, W.S. & Eliceiri, K.W. NIH Image to ImageJ: 25 years of image analysis. *Nat Methods* **9**, 671-675 (2012).

115. Gorzelanny, C., Poppelmann, B., Pappelbaum, K., Moerschbacher, B.M. & Schneider, S.W. Human macrophage activation triggered by chitotriosidase-mediated chitin and chitosan degradation. *Biomaterials* **31**, 8556-8563 (2010).

116. Kalagara, T. *et al.* The endothelial glycocalyx anchors von Willebrand factor fibers to the vascular endothelium. *Blood Adv* **2**, 2347-2357 (2018).

117. Ran, F.A. *et al.* Genome engineering using the CRISPR-Cas9 system. *Nature protocols* **8**, 2281-2308 (2013).

118. Richter, U. *et al.* Adhesion of small cell lung cancer cells to E- and P-selectin under physiological flow conditions: implications for metastasis formation. *Histochemistry and cell biology* **135**, 499-512 (2011).

119. Starzonek, S. *et al.* Systematic analysis of the human tumor cell binding to human vs. murine E- and P-selectin under static vs. dynamic conditions. *Glycobiology* **30**, 695-709 (2020).

120. Giaever, I. & Keese, C.R. Micromotion of mammalian cells measured electrically. *Proceedings of the National Academy of Sciences* **88**, 7896 (1991).

121. Becke, T.D. *et al.* Covalent Immobilization of Proteins for the Single Molecule Force Spectroscopy. *Journal of visualized experiments : JoVE* (2018).

122. Lin, D.C. & Horkay, F. Nanomechanics of polymer gels and biological tissues: A critical review of analytical approaches in the Hertzian regime and beyond. *Soft matter* **4**, 669-682 (2008).

123. Presto, J. *et al.* Heparan sulfate biosynthesis enzymes EXT1 and EXT2 affect NDST1 expression and heparan sulfate sulfation. *Proc Natl Acad Sci U S A* **105**, 4751-4756 (2008).

124. Shively, J.E. & Conrad, H.E. Formation of anhydrosugars in the chemical depolymerization of heparin. *Biochemistry* **15**, 3932-3942 (1976).

125. Gockel, L.M. *et al.* Inhibition of Tumor–Host Cell Interactions Using Synthetic Heparin Mimetics. *ACS Applied Materials & Interfaces* **13**, 7080-7093 (2021).

126. Burke, P.A. *et al.* Cilengitide Targeting of α_vβ₃ Integrin Receptor Synergizes with Radioimmunotherapy to Increase Efficacy and Apoptosis in Breast Cancer Xenografts. *Cancer Research* **62**, 4263-4272 (2002).

127. Pavlov, G., Finet, S., Tatarenko, K., Korneeva, E. & Ebel, C. Conformation of heparin studied with macromolecular hydrodynamic methods and X-ray scattering. *European biophysics journal : EBJ* **32**, 437-449 (2003).

128. Paszek, M.J. *et al.* The cancer glycocalyx mechanically primes integrin-mediated growth and survival. *Nature* **511**, 319-325 (2014).

129. Cerami, E. *et al.* The cBio cancer genomics portal: an open platform for exploring multidimensional cancer genomics data. *Cancer Discov* **2**, 401-404 (2012).

130. Gockel, L.M. *et al.* Inhibition of Tumor-Host Cell Interactions Using Synthetic Heparin Mimetics. *ACS Appl Mater Interfaces* **13**, 7080-7093 (2021).

131. Burgos-Bravo, F., Martínez-Meza, S., Quest, A.F.G., Wilson, C.A.M. & Leyton, L. Application of Force to a Syndecan-4 Containing Complex With Thy-1-α(V)β(3) Integrin Accelerates Neurite Retraction. *Frontiers in molecular biosciences* **7**, 582257 (2020).

132. Singh, I. *et al.* Solution structure of human von Willebrand factor studied using small angle neutron scattering. *The Journal of biological chemistry* **281**, 38266-38275 (2006).

133. Zhang, X., Craig, S.E., Kirby, H., Humphries, M.J. & Moy, V.T. Molecular basis for the dynamic strength of the integrin alpha4beta1/VCAM-1 interaction. *Biophysical journal* **87**, 3470-3478 (2004).

134. Merkel, R., Nassoy, P., Leung, A., Ritchie, K. & Evans, E. Energy landscapes of receptor-ligand bonds explored with dynamic force spectroscopy. *Nature* **397**, 50-53 (1999).

135. Mulloy, B. The specificity of interactions between proteins and sulfated polysaccharides. *Anais da Academia Brasileira de Ciencias* **77**, 651-664 (2005).

136. Barbouri, D. *et al.* Syndecans as modulators and potential pharmacological targets in cancer progression. *Front Oncol* **4**, 4 (2014).

137. Blackhall, F.H., Merry, C.L., Davies, E.J. & Jayson, G.C. Heparan sulfate proteoglycans and cancer. *Br J Cancer* **85**, 1094-1098 (2001).

138. De Pasquale, V. & Pavone, L.M. Heparan Sulfate Proteoglycan Signaling in Tumor Microenvironment. *International Journal of Molecular Sciences* **21**, 6588 (2020).

139. Carnachan, S.M. & Hinkley, S.F.R. Heparan Sulfate Identification and Characterisation: Method II. Enzymatic Depolymerisation and SAX-HPLC Analysis to Determine Disaccharide Composition. *Bio Protoc* **7**, e2197 (2017).

140. Huck, V., Schneider, M.F., Gorzelanny, C. & Schneider, S.W. The various states of von Willebrand factor and their function in physiology and pathophysiology. *Thromb Haemost* **111**, 598-609 (2014).

141. Bret, C. *et al.* Expression of genes encoding for proteins involved in heparan sulphate and chondroitin sulphate chain synthesis and modification in normal and malignant plasma cells. *British journal of haematology* **145**, 350-368 (2009).

142. Collins, L.E. & Troeberg, L. Heparan sulfate as a regulator of inflammation and immunity. *Journal of leukocyte biology* **105**, 81-92 (2019).

143. Martinez, P. *et al.* Macrophage polarization alters the expression and sulfation pattern of glycosaminoglycans. *Glycobiology* **25**, 502-513 (2015).

144. Fiore, V.F., Ju, L., Chen, Y., Zhu, C. & Barker, T.H. Dynamic catch of a Thy-1-alpha5beta1+syndecan-4 trimolecular complex. *Nat Commun* **5**, 4886 (2014).

145. Beauvais, D.M., Burbach, B.J. & Rapraeger, A.C. The syndecan-1 ectodomain regulates alphavbeta3 integrin activity in human mammary carcinoma cells. *The Journal of cell biology* **167**, 171-181 (2004).

146. Obermeier, H.L. *et al.* The role of ADAMTS-13 and von Willebrand factor in cancer patients: Results from the Vienna Cancer and Thrombosis Study. *Research and Practice in Thrombosis and Haemostasis* **3**, 503-514 (2019).

147. Martin, O.A., Anderson, R.L., Narayan, K. & MacManus, M.P. Does the mobilization of circulating tumour cells during cancer therapy cause metastasis? *Nat Rev Clin Oncol* **14**, 32-44 (2017).

148. Joosse, S.A. *et al.* Tumor-Associated Release of Prostatic Cells into the Blood after Transrectal Ultrasound-Guided Biopsy in Patients with Histologically Confirmed Prostate Cancer. *Clinical Chemistry* **66**, 161-168 (2019).

Acknowledgments

First, I owe my great gratitude to Prof. Dr. med. Stefan W. Schneider, for giving me the opportunity to carry out this thesis in their research group. Thank you for your advice, for your helpful discussions. Besides, I would like to thank Prof. Dr. Viktor Umansky, who made this thesis possible being my first supervisor. Moreover, I want to thank the three members of my thesis advisory committee. Thank you for taking your precious time to let me defend my work.

In particular, I would like to express my deepest appreciation to Dr. Christian Gorzelanny who supervised me through this PhD thesis. He always had a helping hand when I needed one both at work and in my life. He allowed me to push my project further than I ever imagined. I could not be able to do this without him and for that, I am forever grateful.

A great thanks also go to Dr. Alex Thomas Bauer who gave me helpful discussions and helped me with all the animal experiments and the amazing results were crucial for the progress of this thesis. In addition, I would like to thank Dr. Xiaobo Liu for his scientific support and suggestions.

Thanks to all my lab colleagues at Mannheim and Hamburg for the great atmosphere, their helpful advice, support and their friendship: Dr. Volker Huck , Christian Meß, Natalia Halter , Sabine Vidal, Ewa Wladykowski , Tobias Obser, Dr. José Robador; Dr. Gustavo RamosGustavo Ramos, Dr. Lydia von Palubitzki , Mina Zulal, Laura Adam, Antonia Burmeister. I would like to thank our cooperation partners: Prof.Dr. Gerd Bendas and Martin Heyes at the University of Bonn for performing SAW experiment. Prof. Dr. Marion Kusche-Gullberg at the University of Bergen for performing gel chromatography experiment. Prof.Dr. Tobias Lange, Sarah Starzonek, Prof.Dr. Sabine Riethdorf and Leonie Ott in UKE hamburg.

To the love of my life, my husband. I will not find the right words to describe how grateful I am for you being by my side. Thank you for your great help with my work and thank you for your dedication to our family. Special thanks to my son. Thanks for being my boy, thanks for making me smile every single day with you.

Finally, I would like to thank my family and friends in China. They all supported me and have given me unconditional encouragement throughout. I would not have been able to complete the PhD without them.